

FINAL REPORT

HIGH PERFORMANCE SOLID ROCKET MOTOR (SRM) SUBMERGED NOZZLE/COMBUSTION CAVITY FLOWFIELD ASSESSMENT

22 December 1987

Contract NAS8-35980

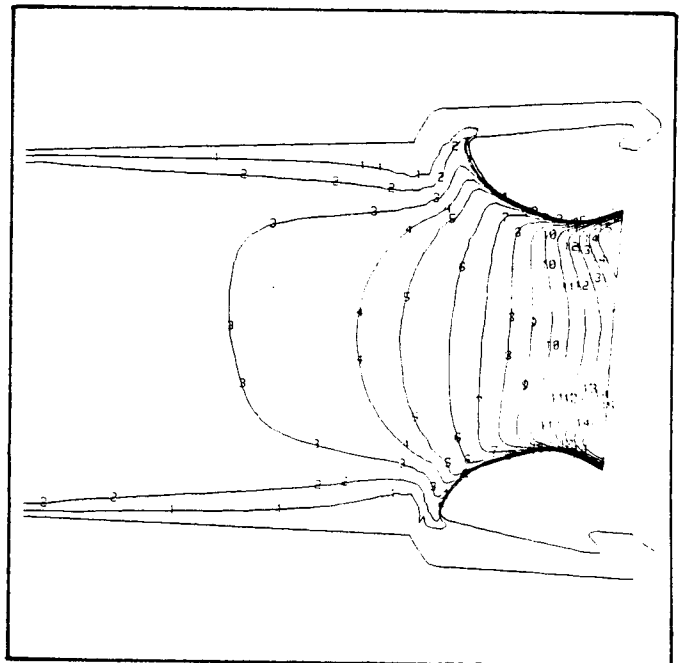
Prepared by

J.A. Freeman

J.S. Chan

J.E. Murph

K.E. Xiques



 **Lockheed**
Missiles & Space Company, Inc.
Huntsville Engineering Center
4800 Bradford Blvd., Huntsville, AL 35807

For

**NATIONAL AERONAUTICS AND SPACE ADMINISTRATION
MARSHALL SPACE FLIGHT CENTER, AL 35812**

(NASA-CR-179367) HIGH PERFORMANCE SOLID
ROCKET MOTOR (SRM) SUBMERGED
NOZZLE/COMBUSTION CAVITY FLOWFIELD
ASSESSMENT Final Report (Lockheed
and Space Co.) 57 p

Missiles
CSCL 21H G3/20 0128298

N88-18622

Unclass

FOREWORD

This final report is submitted by Lockheed Missiles & Space Company, Inc., Huntsville Engineering Center, to the National Aeronautics and Space Administration's George C. Marshall Space Flight Center, Alabama, for Contract NAS8-35980 entitled "High Performance Solid Rocket Motor (SRM) Submerged Nozzle/Combustion Cavity Flowfield Assessment."

The NASA-MSFC Contracting Officer's Representative for this contract was Dr. Terry F. Greenwood, ED33, Chief of the Induced Environment Branch, Aerophysics Division, of the Structures and Dynamics Laboratory.

ACKNOWLEDGEMENT

The authors gratefully acknowledge the guidance for this effort provided by the NASA-MSFC technical monitor, Dr. Terry F. Greenwood. Also, the valuable assistance and contributions of the following individuals are acknowledged:

At the Lockheed-Huntsville Engineering Center:

- Alan Nicholson, Orgn. 59-91, 3D Grid Generation
- Don Hanline, Orgn. 59-91, 3D Flowfield Initialization
- Mike Robinson, Orgn. 59-91, CFD Technical Consultation
- Ron Jewell, Orgn. 59-91, Flowfield Plotting

At Morton Thiokol, Inc., Space Division:

- Dennis Bright, 3D Gimbaled Nozzle Geometry Definition

At the NASA Marshall Space Flight Center, Aerophysics Division:

- Dana Billings, 2D Nozzle Grid Construction Consultation.

SUMMARY

Two- and three-dimensional internal flowfield solutions for critical points in the Space Shuttle solid rocket booster burn time have been developed using the Lockheed Huntsville GIM/PAID Navier-Stokes solvers. These perfect gas, viscous solutions for the high performance motor characterize the flow in the aft segment and nozzle of the booster. Two-dimensional axisymmetric solutions have been developed at $t = 20$ and $t = 85$ sec motor burn times. The $t = 85$ sec solution indicates that the aft segment forward inhibitor stub produces vortices which are shed and convected downstream. Vortex shedding may be a source of the acoustic activity noted in the flight and static test history of the Space Shuttle solid rocket boosters. The $t = 20$ sec two-dimensional axisymmetric solution does not predict the occurrence of vortex shedding within the motor aft segment.

A three-dimensional 3.5-deg gimbaled nozzle flowfield solution has been developed for the aft segment and nozzle at $t = 9$ sec motor burn time. This perfect gas, viscous analysis, provided a steady state solution for the core region and the flow through the nozzle, but indicates that unsteady flow exists in the region under the nozzle nose and near the flexible boot and nozzle/case joint. The flow in the nozzle/case joint region is characterized by low magnitude (less than 1.0 psia differential) pressure waves which travel in the circumferential direction. The calculation predicts a circumferential surface static pressure differential at the nozzle/case joint of approximately 0.55 psia.

From the two- and three-dimensional flowfield calculations presented in this report it can be concluded that there is no evidence from these results that steady state gas dynamics is the primary mechanism resulting in the nozzle pocketing erosion experienced on SRM nozzles -8A or -17B. The steady state flowfield results indicate pocketing erosion is not directly initiated by a steady state gas dynamic phenomenon.

CONTENTS

<u>Section</u>	<u>Page</u>
FOREWORD	ii
ACKNOWLEDGEMENT	iii
SUMMARY	iv
1 INTRODUCTION	1
2 HIGH PERFORMANCE MOTOR GASDYNAMIC ANALYSES	3
2.1 Two-Dimensional Axisymmetric HPM Aft Segment/ Nozzle Flow Fields	4
2.1.1 HPM Aft Segment/Nozzle Flow Field at t = 85 sec	4
2.1.2 HPM Aft Segment/Nozzle Flow Field at t = 20 sec	13
2.1.3 Comparison of the Axisymmetric HPM Flowfield Calculations at t = 20 and 85 sec	13
2.2 Three-Dimensional HPM 3.5-deg Gimbaled Nozzle Flow Field at t = 9 sec	28
2.2.1 Computational Grid and Initial Conditions	28
2.2.2 HPM Nozzle/Combustion Cavity Flowfield Computation and Results	28
2.2.3 HPM Nozzle/Case Joint Region Flowfield Computation and Results	32
3 CONCLUSIONS	49
3.1 Findings of the 2D Axisymmetric Steady State Gasdynamic Analysis	50
3.2 Findings of the 3D 3.5-deg Gimbaled Nozzle Steady State Gasdynamic Analysis	50
REFERENCES	51
DISTRIBUTION	

1. INTRODUCTION

The NASA Space Shuttle, which has been termed Space Transportation System (STS), utilizes solid rocket boosters in the ascent phase propulsion system. The Space Shuttle Solid Rocket Boosters, during their development, qualification and flight firings, have periodically experienced unusual pocketing erosion patterns in the tape-wrapped carbon phenolic nozzle components, of the forward nose section [(forward nose ring (403), the aft inlet ring (404)], and the throat ring. The assessment of the combination of factors which contribute to what is termed "pocket erosion" is the subject of extensive investigation by the Solid Rocket Motor community.

A High Performance Solid Rocket Motor (HPM) has been incorporated into the system and two of these new motors first flew on Flight STS-8. Post-flight inspection of HPM nozzle hardware revealed greater than expected nozzle erosion on the 403 and 404 rings of nozzle 8A, while erosion on nozzle 8B was nominal. During the flight of STS-51D abnormal nozzle erosion occurred in the throat ring of SRM-17B just downstream of the nozzle throat. This was the first and only occurrence of significant "pocket erosion" in the nozzle throat ring. The physical characteristics of the observed erosion on nozzles 8A and 17B are similar except for axial location. The difference in observed erosion between nozzles 8A and 8B points to a material or fabrication problem with nozzle 8A. Another possibility is that a contributing factor to the erosion could have been a gasdynamic phenomenon in the combustion cavity/submerged nozzle flow field.

The objective of this effort is to determine the steady state flow field within the HPM combustion cavity during critical periods in the motor burn time and to determine the nozzle fluid/thermal environment. The gasdynamic analyses presented provide an assessment of the nozzle steady state flow field and its contribution to the observed nozzle "pocket erosion."

This effort was divided into two major subtasks: the calculation of two- and three-dimensional HPM flowfields. Some of the results presented in this report were obtained in parallel with the gasdynamic analysis tasks conducted under NASA-MSFC Contract NAS8-36197. The two-dimensional axisymmetric HPM aft segment/nozzle flowfields and preliminary results from the three-dimensional 3.5-deg gimbaled nozzle internal flowfield at $t = 9$ sec have been previously reported in the final report for Contract NAS8-36197 (Ref. 1). These results are included in this report with an expanded discussion for the sake of completeness.

Also presented in this report is the computation of the three-dimensional flowfield in the HPM nozzle/case joint region including a calculation of the circumferential static pressure gradient at the nozzle/case joint surface for a 3.5-deg gimbaled nozzle at $t = 9$ sec motor burn time.

Section 2 of the report presents the technical discussion and results of the gasdynamic analyses and Section 3 presents the conclusions of the study.

2. HIGH PERFORMANCE MOTOR GASDYNAMIC ANALYSES

Sections 2.1 and 2.2 present the results of the High Performance Motor (HPM) nozzle gasdynamic analyses performed by personnel of the Computational Mechanics Section at Lockheed's Huntsville Engineering Center. Section 2.1 discusses the results of two-dimensional axisymmetric perfect gas analyses of the steady state internal flow field of the HPM aft segment and nozzle computed at $t = 85$ sec and 20 sec motor burn times. These axisymmetric analyses were conducted by Mr. John S. Chan who constructed the computational grid and performed the flowfield integration to provide the steady state solutions presented.

Section 2.2 discusses the results of the three-dimensional perfect gas analysis of the HPM aft segment gimbaled nozzle flow field for a 3.5-deg nozzle gimbal angle at $t = 9$ sec motor burn time. The three-dimensional gimbaled nozzle computational grid was constructed by Mr. Jesse E. Murph who also computed the initialization for the three-dimensional gimbaled nozzle flowfield calculation. The flowfield integration was performed initially by Mr. Ken E. Xiques and completed by Mr. Jon A. Freeman. Section 2.2 also discusses the results of the three-dimensional perfect gas analysis of the flow in the nozzle/case joint region for a 3.5-deg gimbaled nozzle at $t = 9$ sec.

The two-dimensional flowfield results were obtained using the Lockheed-Huntsville General Interpolants Method (GIM) code and the three-dimensional results were obtained using the Lockheed-Huntsville Progressive Assembly of Interpolated Differences (PAID) code. The gas properties and initial conditions used in both the two- and three-dimensional gasdynamic analyses to initialize the flowfield calculations were obtained from the NASA-MSFC Space Shuttle SRM one-dimensional internal ballistics calculation provided by Charles L. Martin, EP54 (Ref. 2).

2.1 TWO-DIMENSIONAL AXISYMMETRIC HPM AFT SEGMENT/NOZZLE FLOW FIELDS

A cutaway view of the Space Shuttle Solid Rocket Booster is shown in Fig. 1. The configuration of the HPM aft segment propellant boundary and forward inhibitor stub at motor burn times $t = 0, 20, \text{ and } 85 \text{ sec}$ are shown in Fig. 2. The inhibitor stub heights versus burn time were obtained from Ref. 3. These figures indicate the general configurations of the HPM combustion cavity and nozzle regions for which two-dimensional axisymmetric flowfield solutions were developed. The two-dimensional axisymmetric flowfield calculations were carried out assuming no mass addition from the propellant burning surface and a laminar fluid viscosity.

2.1.1 HPM Aft Segment/Nozzle Flow Field at $t = 85 \text{ sec}$

The GIM code grid layout for the entire region and gas properties are shown in Fig. 3. Figures 4 and 5 show the detailed grid of the aft segment forward inhibitor region and nozzle region, respectively. The total number of grid points used in the computation is 13,019.

The $t = 85\text{-sec}$ computation was carried out to 30,000 iterations. At this point in the relaxation process, the flow over the nozzle 402/403/404 rings and through the throat had reached a steady state solution. However, the regions just downstream of the forward inhibitor stub and under the nozzle nose still exhibited unsteady behavior at iteration 30,000. The Mach number and static pressure (P/P_0) contours for the aft segment and nozzle are shown in Figs. 6 and 7, respectively. The static pressure contours shown in Fig. 7 are normalized by the inlet plane stagnation pressure shown in Fig. 3 ($P_0 = 600.333 \text{ psia}$). From these figures, it is evident that the flow over the top of the submerged nozzle and through the nozzle throat is steady and well behaved.

The calculated velocity vector fields just downstream of the forward inhibitor stub for iterations 27,000 and 30,000 are shown in Fig. 8. It is obvious from this figure that the vortex shedding which occurs as a result of the inhibitor stub is captured by the GIM code computation. The vortex

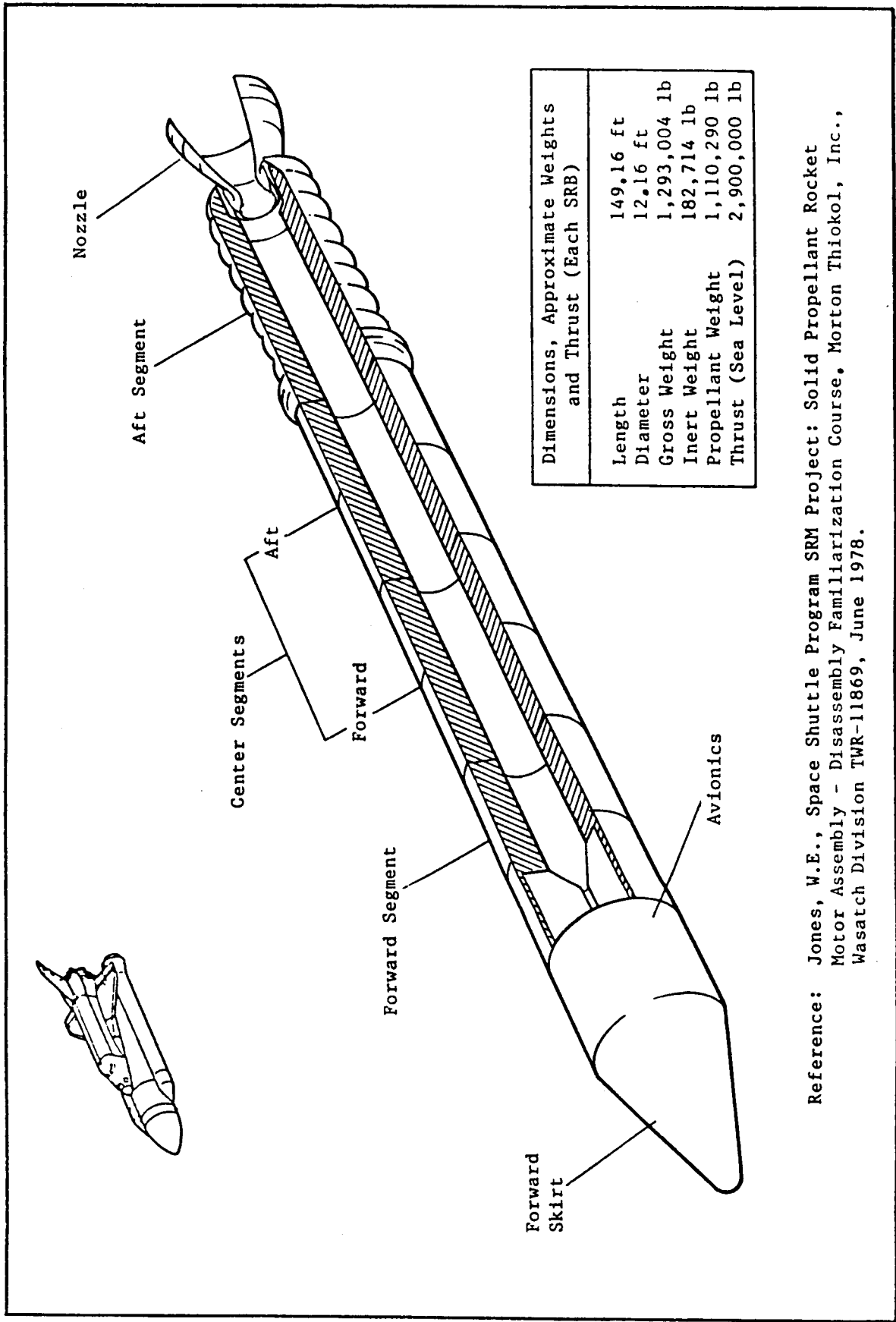


Fig. 1 Pictorial View of the Space Shuttle Solid Rocket Booster

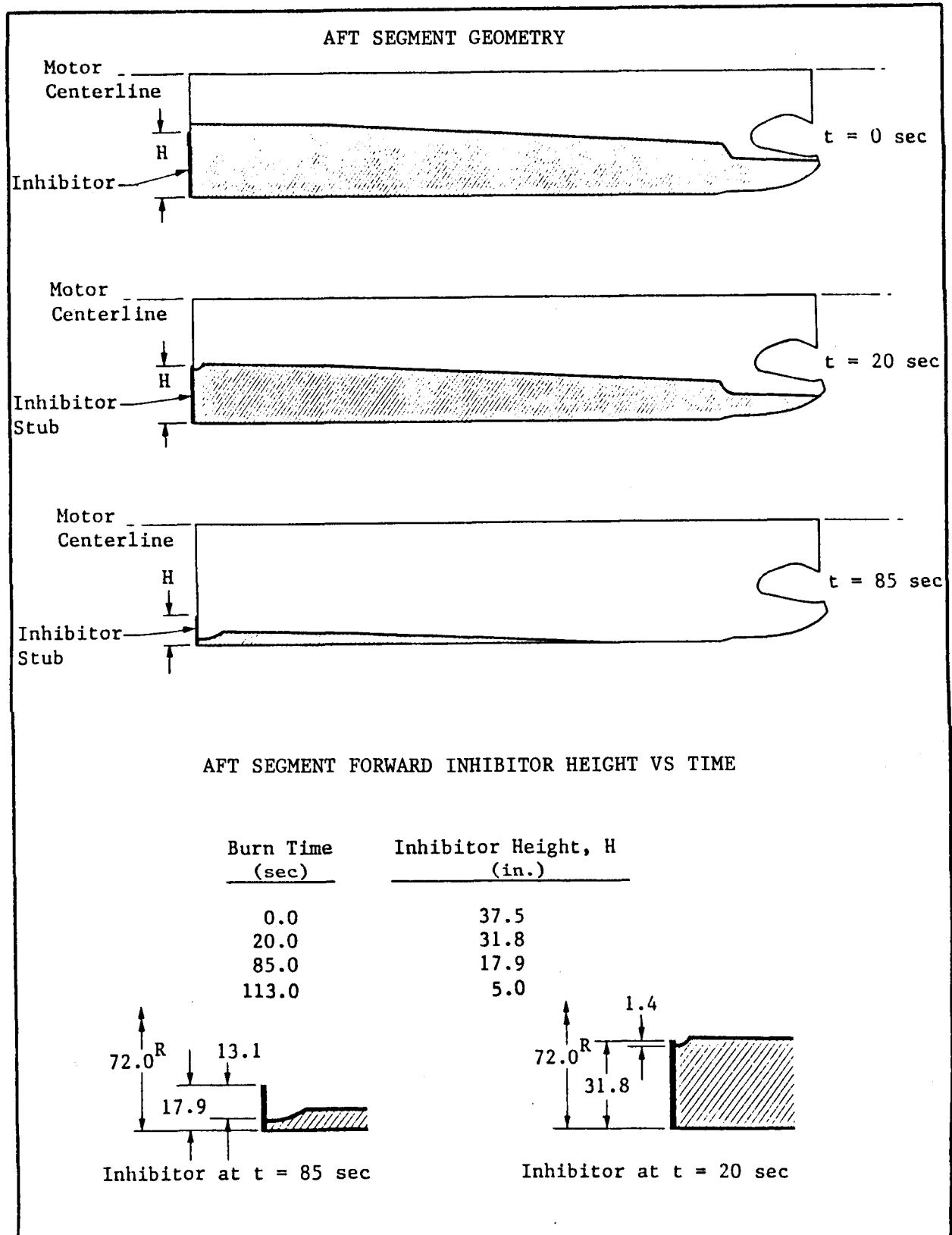


Fig. 2 HPM Aft Segment/Nozzle Geometry at $t = 0$, $t = 20$, and $t = 85$ sec

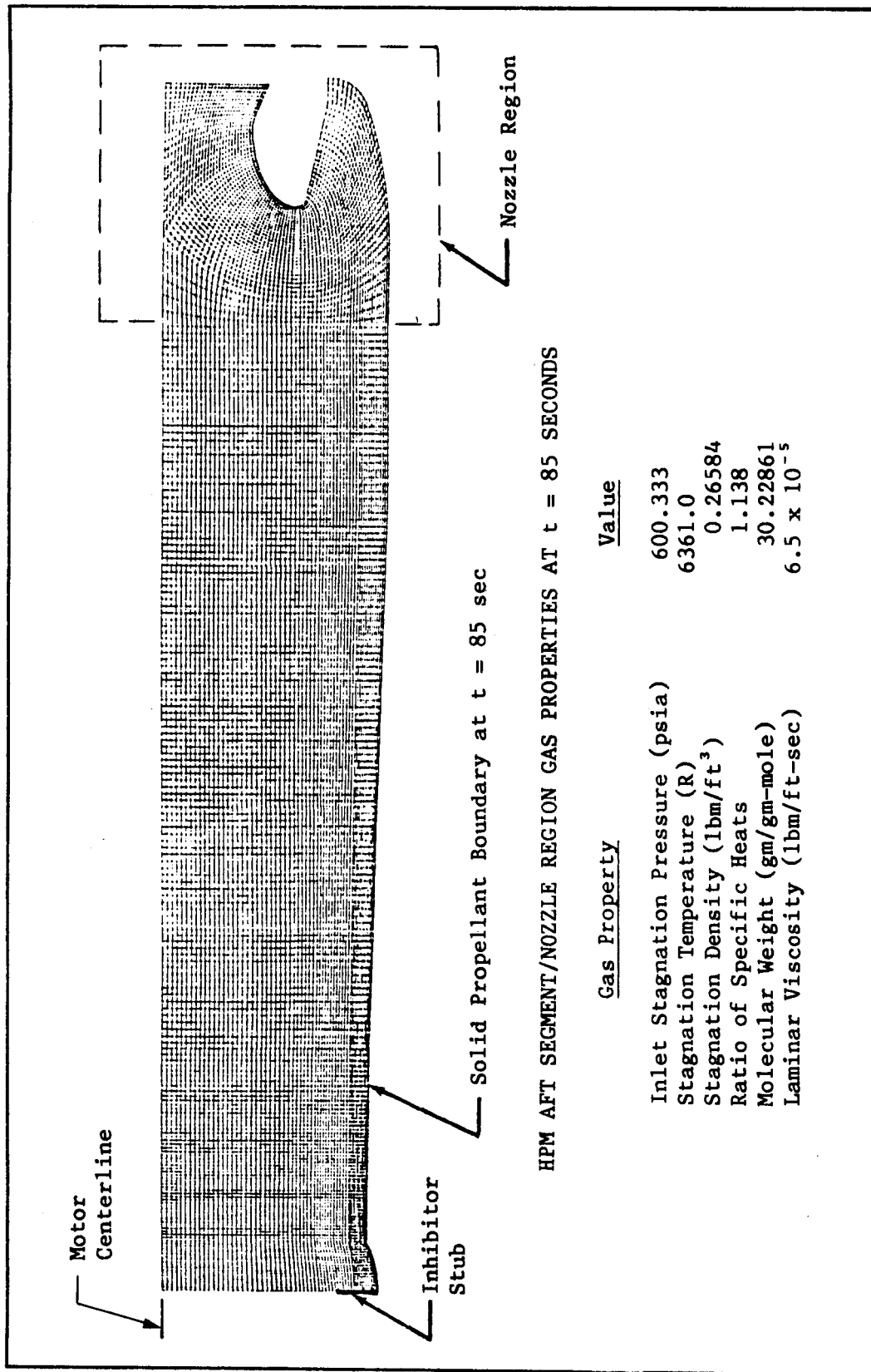


Fig. 3 HPM Aft Segment/Nozzle Geometry and Initial Conditions at $t = 85$ sec

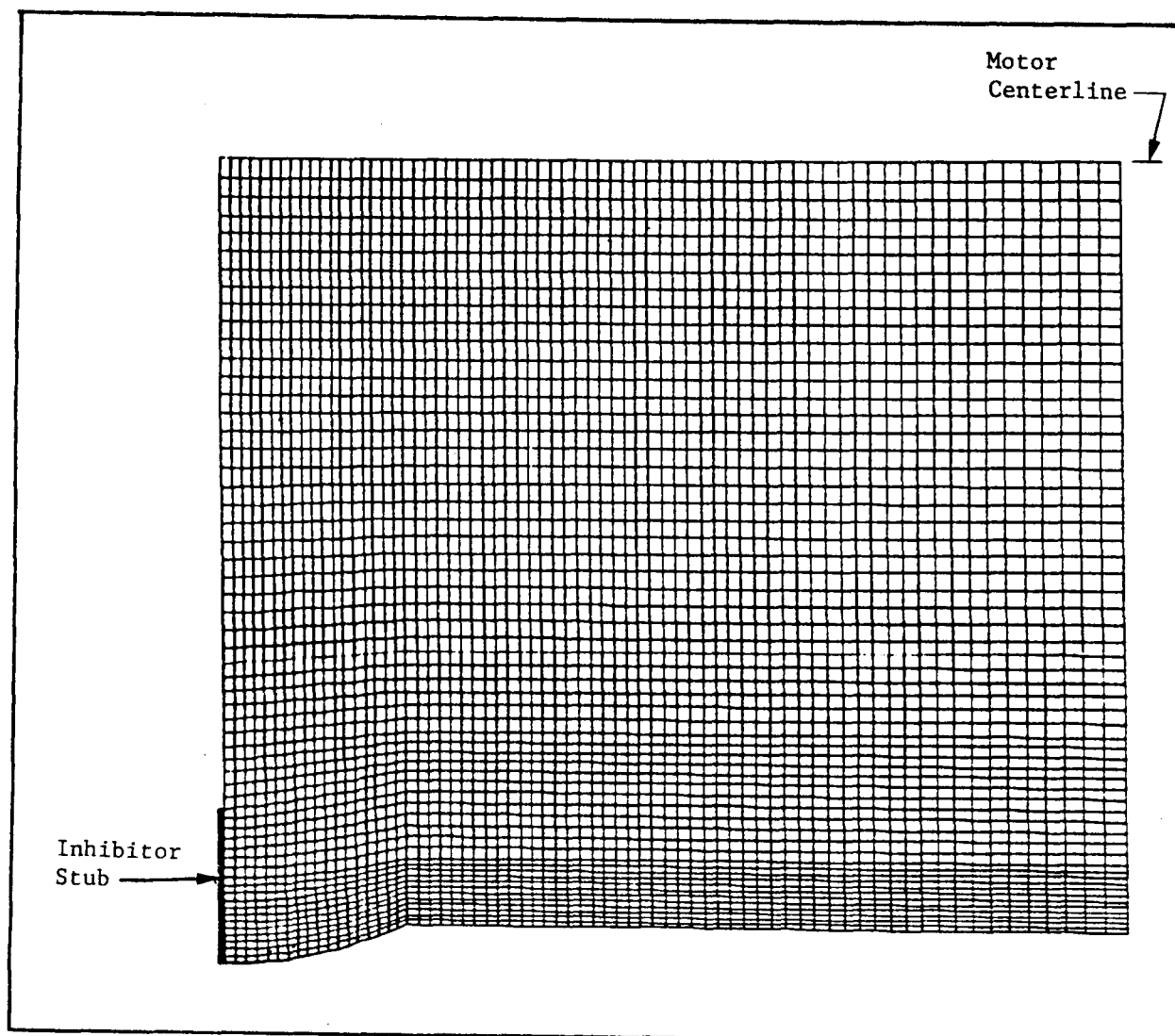


Fig. 4 GIM Code Grid - Region Adjacent to the Aft Segment Inhibitor Stub at $t = 85$ sec

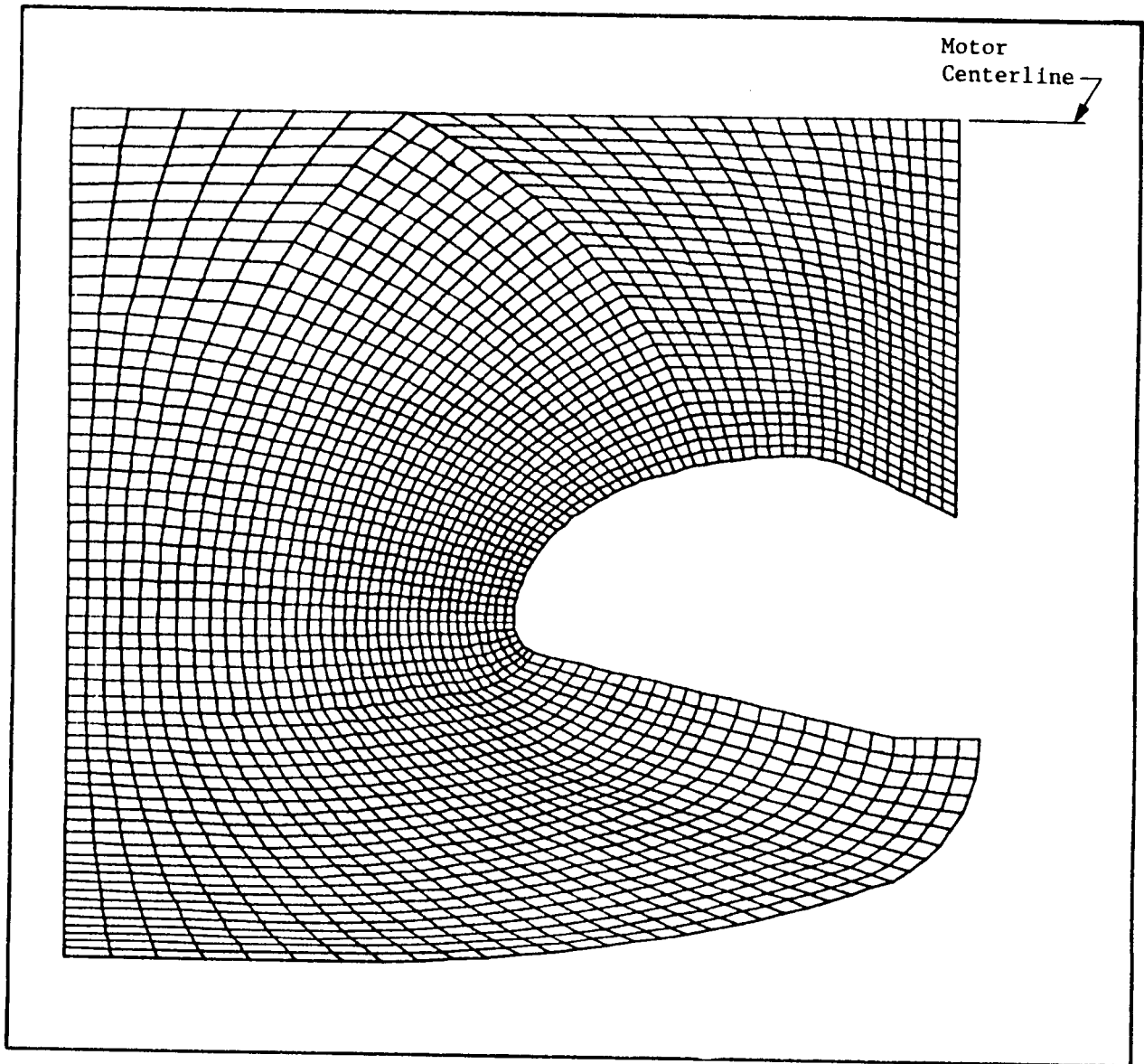


Fig. 5 GIM Code Grid - Nozzle Region at $t = 85$ sec

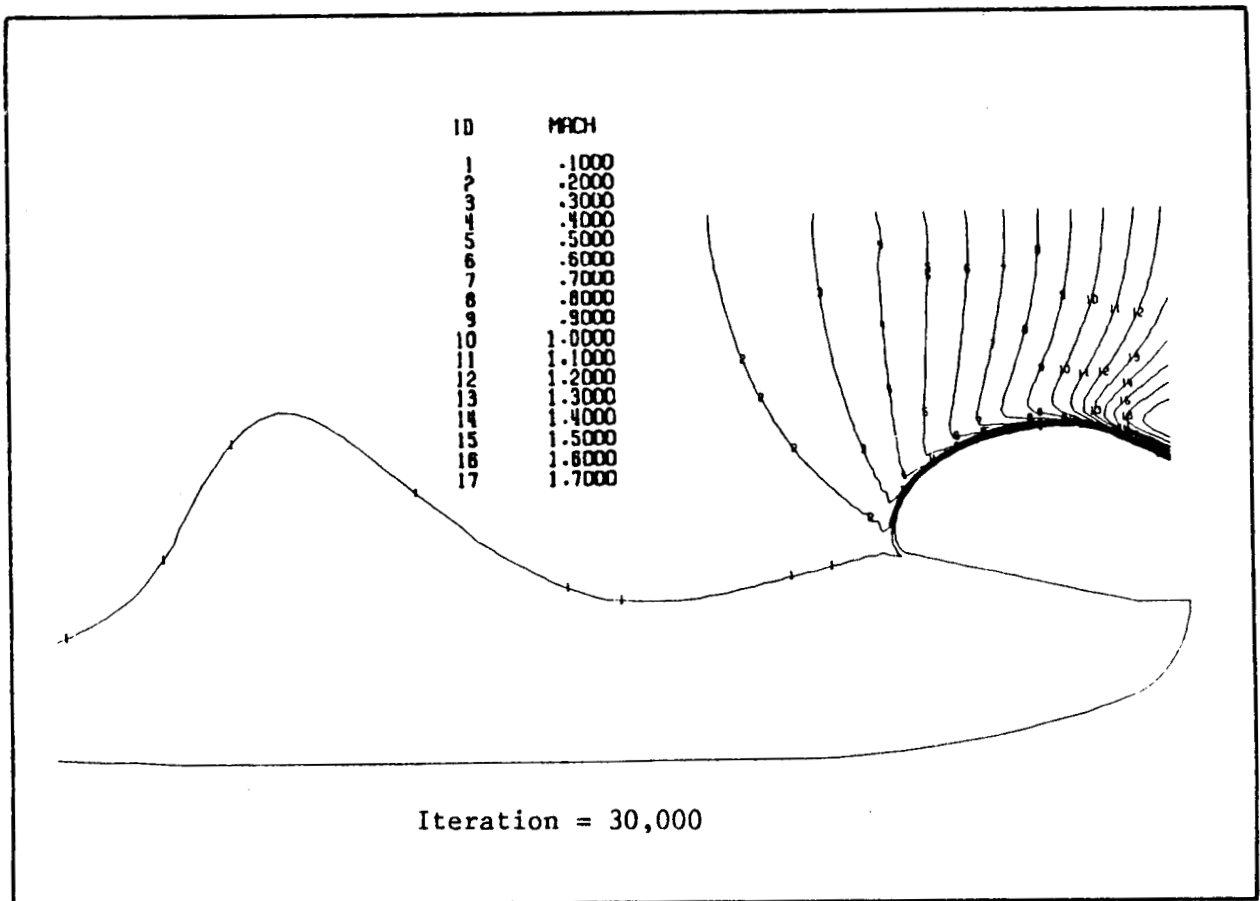


Fig. 6 GIM Code Calculated Mach Number Contours at $t = 85$ sec

PRECEDING PAGE BLANK NOT FILMED

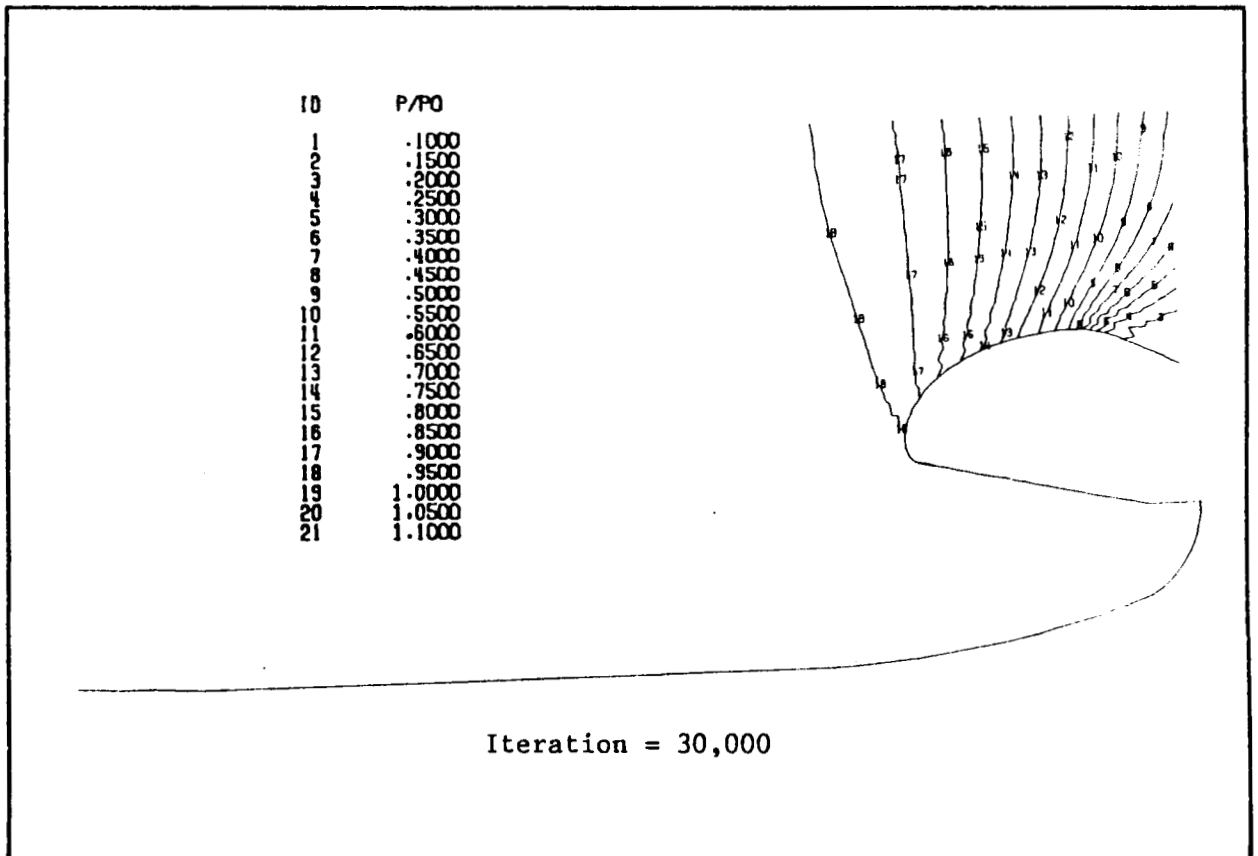


Fig. 7 GIM Code Calculated Static Pressure Contours at $t = 85$ sec

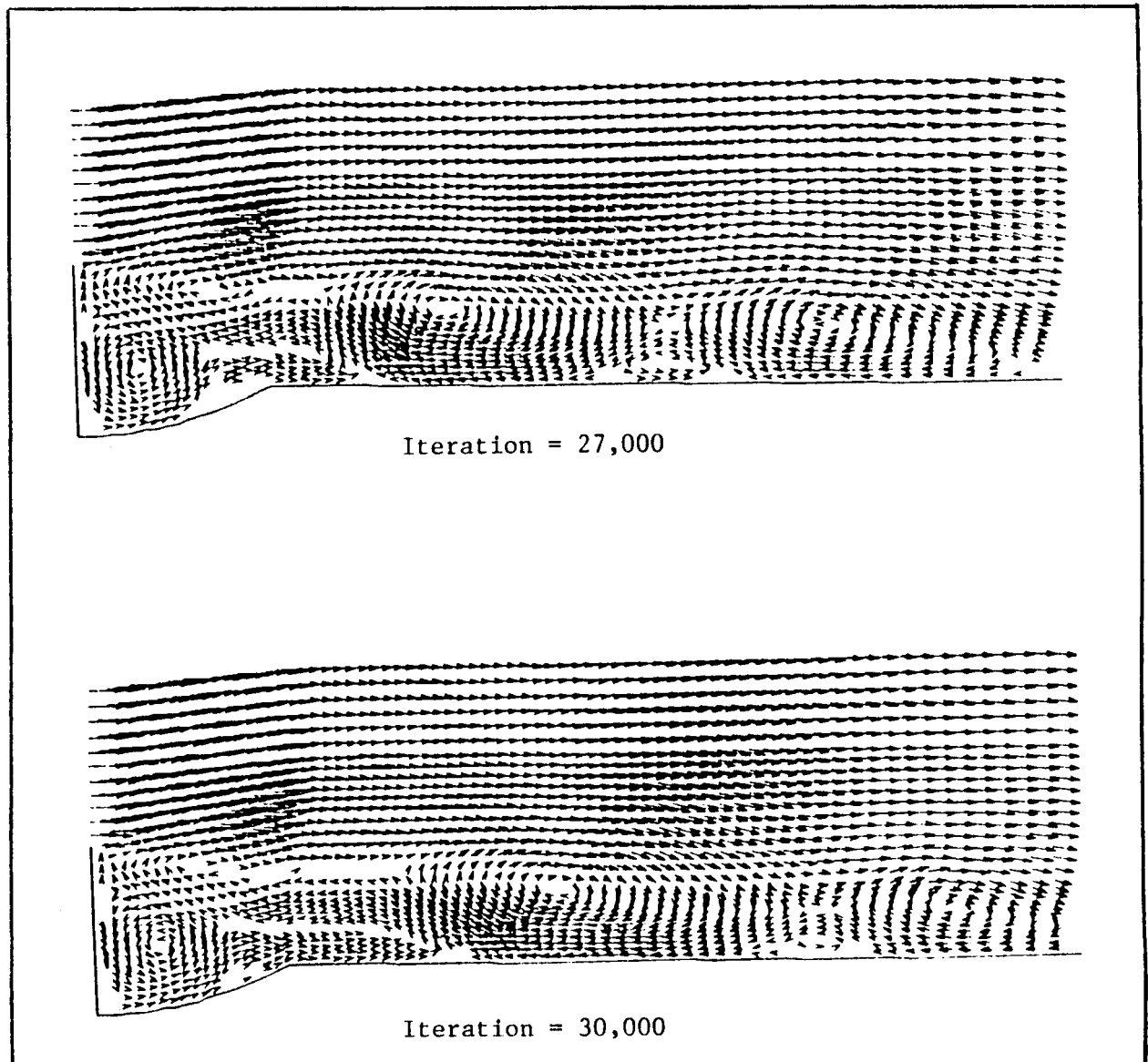


Fig. 8 GIM Code Calculated Velocity Vector Field Adjacent to the Inhibitor Stub at $t = 85$ sec

shedding is an unsteady phenomenon in which the vortices are shed and convected downstream. The velocity vector fields in the cavity under the nozzle nose at iterations 28,000 and 30,000 are shown in Fig. 9. Here, the recirculating flow is clearly shown and the flow pattern is unsteady up to iteration time step 30,000.

2.1.2 HPM Aft Segment/Nozzle Flow Field at $t = 20$ sec

The GIM code grid and gas properties for the $t = 20$ sec calculation are shown in Fig. 10. The total number of grid points used in the computation is 9109, and the grid is similar to the grid used in the $t = 85$ sec calculation.

The $t = 20$ sec computation was carried out to 30,000 iterations. As shown in Fig. 2, the inhibitor stub at $t = 20$ sec does not protrude into the flow field nearly as far as in the $t = 85$ sec configuration. Calculated velocity vector field maps for the regions just downstream of the inhibitor stub and under the nozzle nose are shown in Fig. 11. Notice that near the inhibitor stub there is no evidence of unsteady behavior, i.e., no indication of vortex shedding. In the region under the nozzle nose, unsteady recirculation patterns have developed similar to the $t = 85$ -sec results.

The Mach number and static pressure (P/P_0) contours for the nozzle region are shown in Fig. 12. The static pressure contours shown in Fig. 12 are normalized by the inlet plane stagnation pressure shown in Fig. 10 ($P_0 = 878.936$ psia). From the calculated Mach number and pressure distributions shown in Fig. 12, it is evident that the flow over the top of the submerged nozzle and through the nozzle throat is steady and well behaved.

2.1.3 Comparison of the Axisymmetric HPM Flowfield Calculations at $t = 20$ and 85 sec

The calculated velocity field maps in the inhibitor region are compared in Fig. 13. This figure shows that vortices are not shed from the inhibitor at $t = 20$ sec as they are in the $t = 85$ -sec calculation. The calculated velocity vector field maps in the nozzle nose region are compared in Fig. 14.

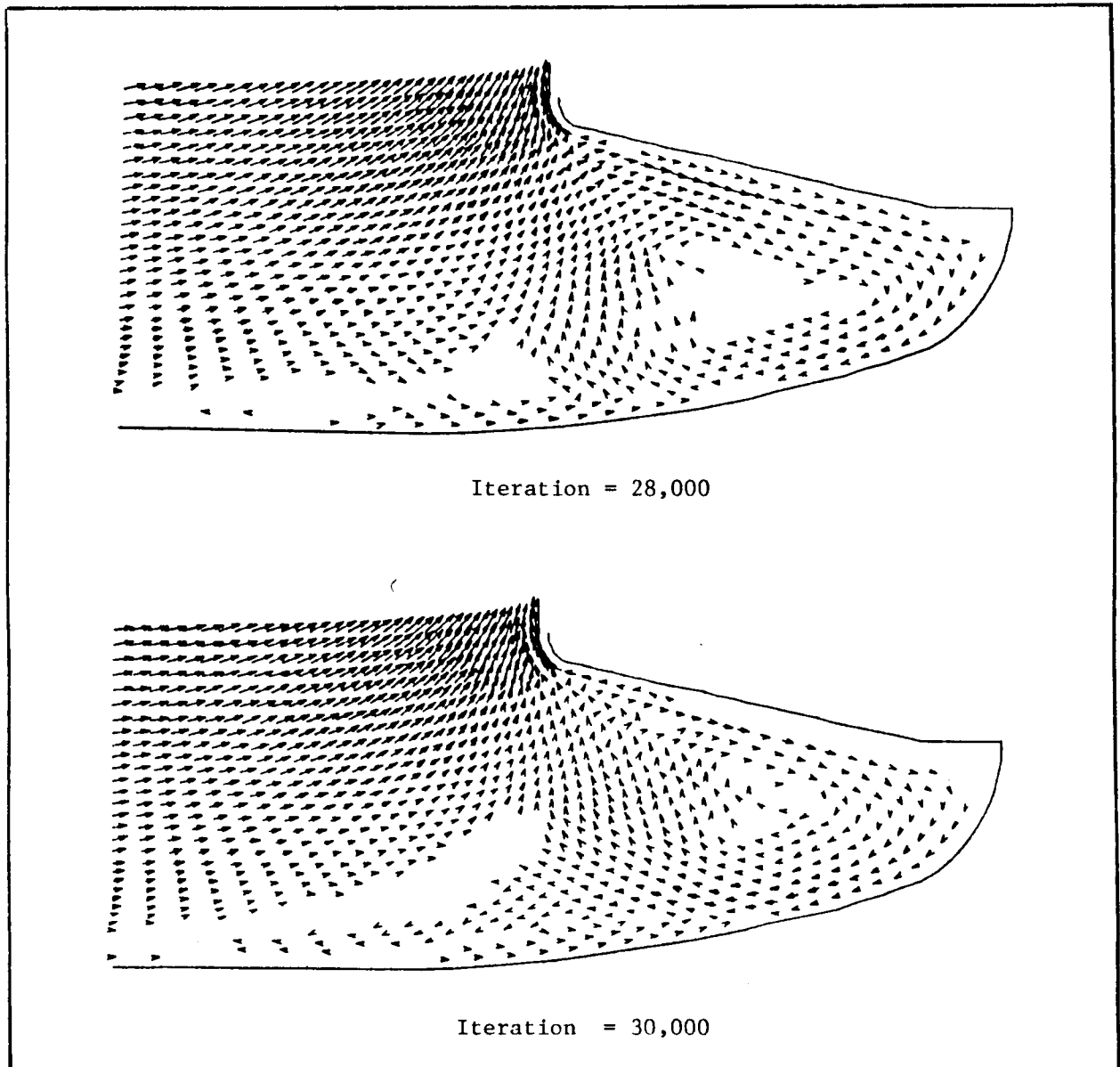


Fig. 9 GIM Code Calculated Velocity Vector Field in Nozzle Region (Lower Part) at $t = 85$ sec

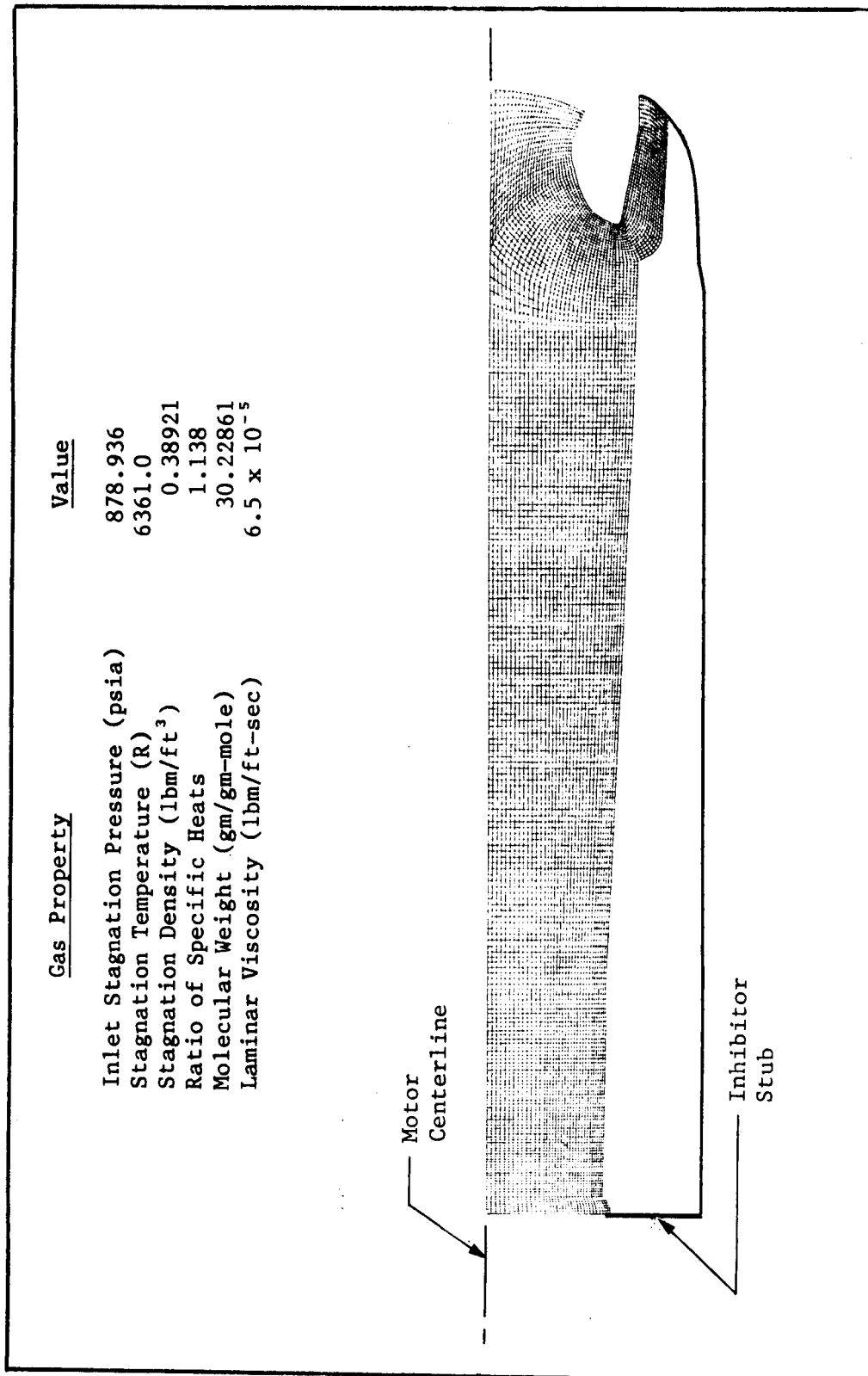


Fig. 10 HPM Aft Segment/Nozzle Geometry GIM Code Grid, and Gas Properties at $t = 20$ sec

PRECEDING PAGE BLANK NOT FILMED

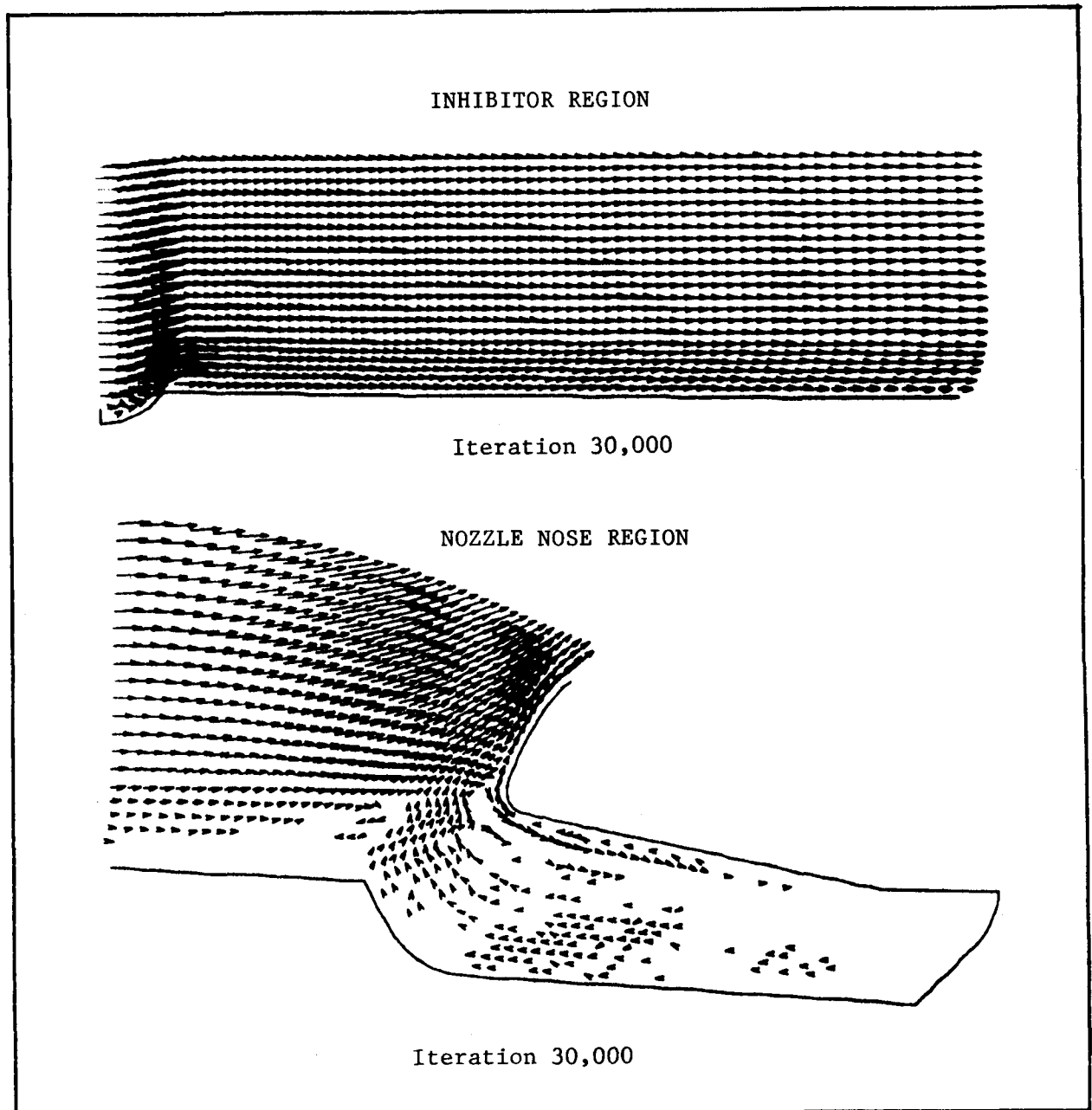
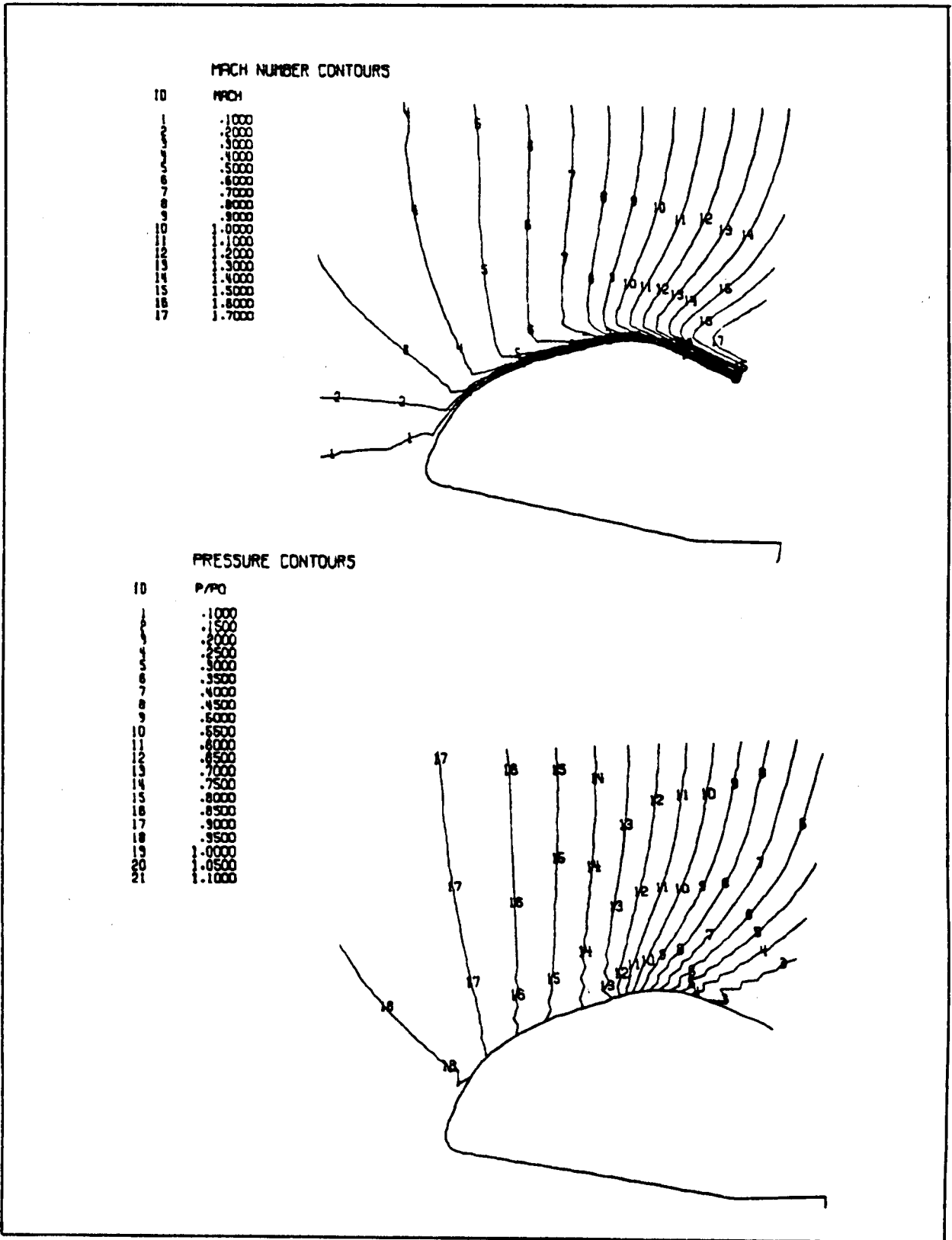


Fig. 11 GIM Code Calculated Velocity Fields, Inhibitor Region and Nozzle Nose Region at $t = 20$ sec

PRECEDING PAGE BLANK NOT FILMED



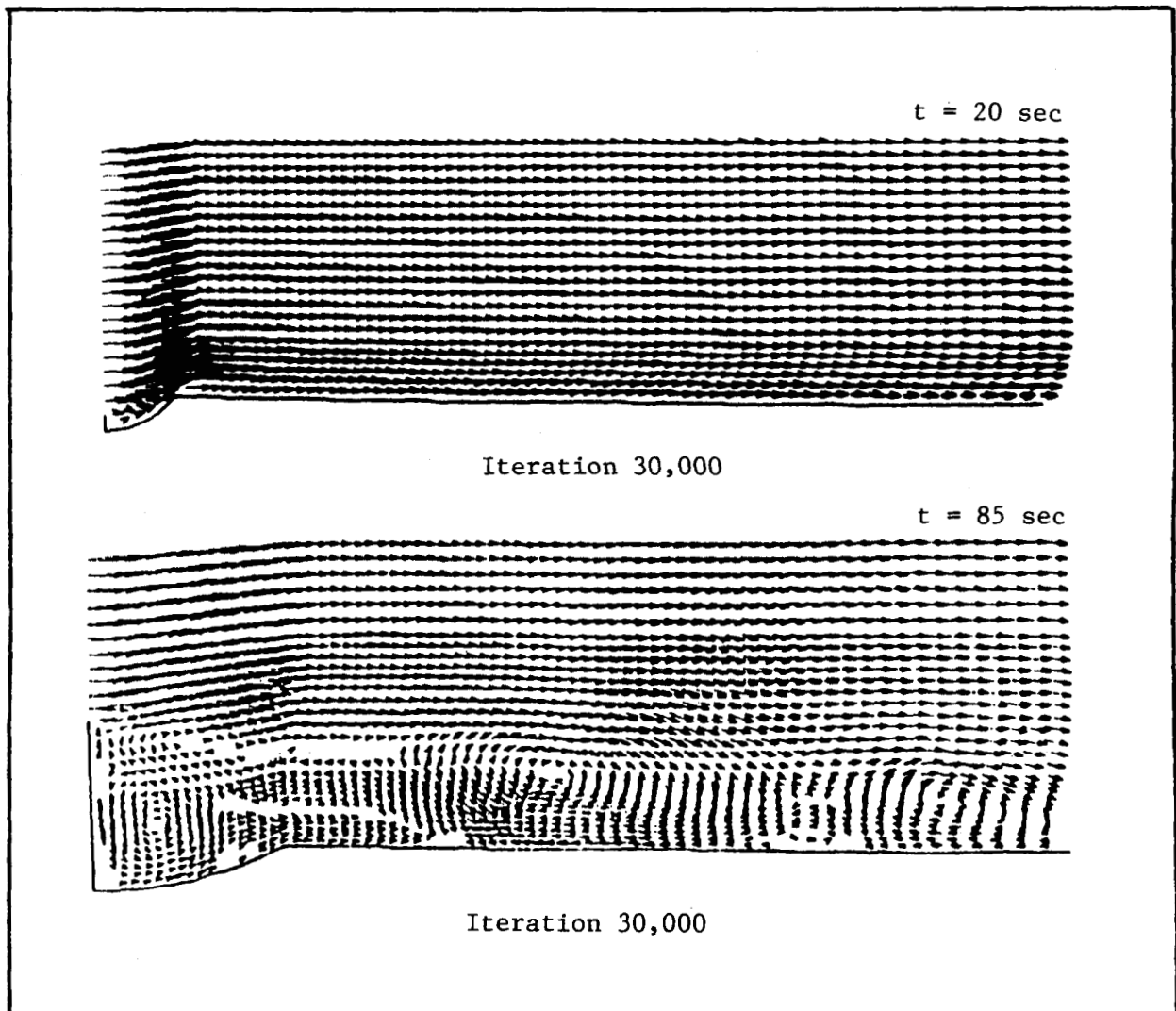


Fig. 13 GIM Code Calculated Velocity Vector Field Comparison (Inhibitor Region)

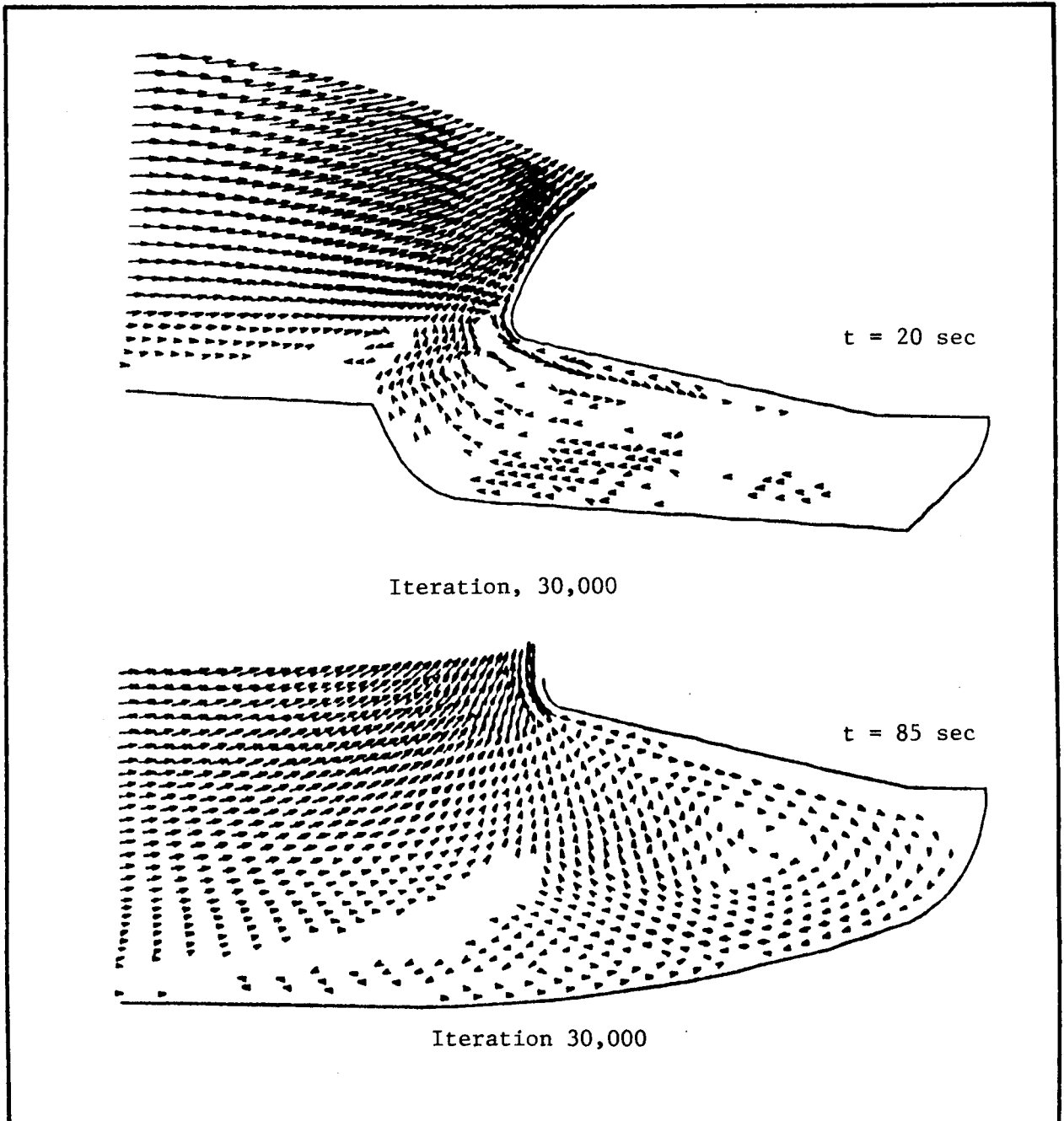


Fig. 14 GIM Code Calculated Velocity Field Comparison - Nozzle Nose Region

Figure 14 demonstrates that quiescent, but unsteady, flow exists under the submerged nozzle nose in both the $t = 20$ and $t = 85$ -sec calculations. The flow under the nozzle nose was investigated in a two-dimensional planar water table experiment conducted by Morton Thiokol, Inc., Wasatch Operations in June 1984 (Ref. 4). The results of this experiment determined qualitatively that recirculating flow is possible under the nozzle nose. The two-dimensional axisymmetric results for the flow under the nozzle nose presented here are in qualitative agreement with the experimental results of Ref. 4.

The approximate location of the separation streamline which divides the unsteady region under the nozzle nose from the steady flow that goes over top of the nozzle nose can be determined from the results of these flowfield calculations. Expanded velocity vector plots are presented in Figs. 15 and 16. These figures show the location of the boundary layer separation along the lower solid boundary as the flow approaches the nozzle nose. Boundary layer separation is observed as the absence of velocity vectors adjacent to the propellant (or case wall) surface. Velocity vectors below the indicated minimums (50 ft/sec for the $t = 20$ sec model, and 38 ft/sec for the $t = 85$ sec model) are not plotted. Therefore, a distinct pattern of rapidly growing boundary layer thickness, i.e., flow separation, is evident. A dashed line on each figure indicates the approximate location of the separation streamline. Note that while the separation points on the upstream solid boundaries occur at approximately the same axial locations, the separation streamlines approach the nozzle nose differently in each case. In Fig. 15 ($t = 20$ sec), the separation streamline is not connected to the nozzle nose since the mass flux from the burning propellant under the nozzle will not allow the streamline to reach the nozzle surface. This propellant mass generation is not included in this model. In Fig. 16 ($t = 85$ sec), the separation streamline is connected to the nozzle nose since no mass generation is present aft of the separation point. Also, since the gases aft of the separation streamline are trapped during steady state flow conditions, the separation streamline approximates the stagnation streamline.

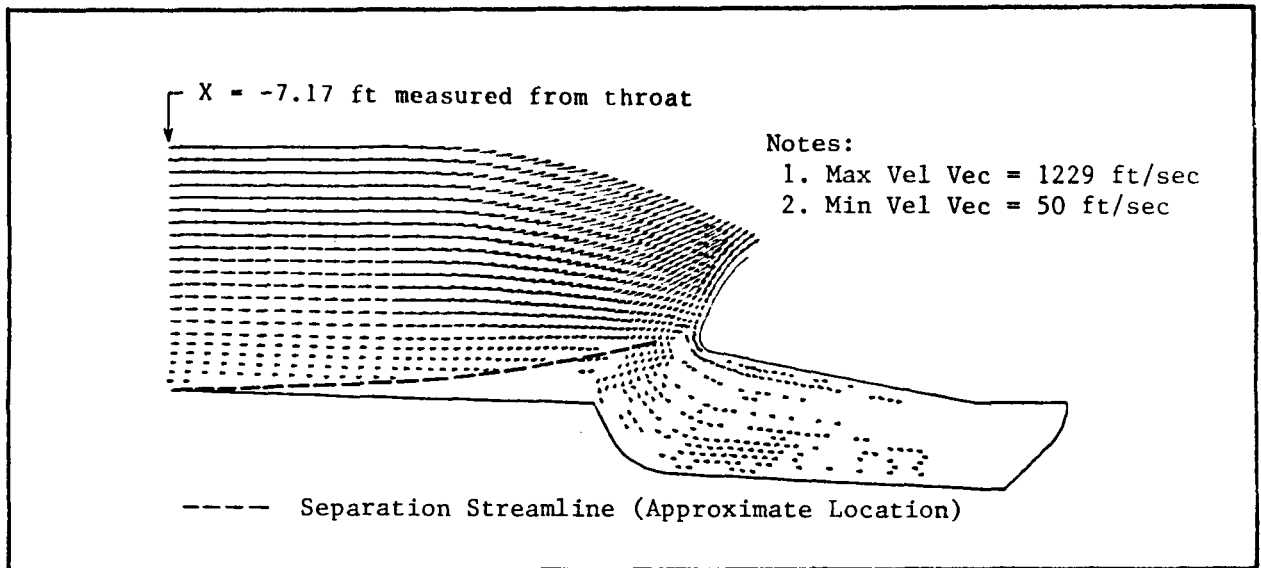


Fig. 15 GIM Code Calculated Velocity Vector Field
at t = 20 sec (Iteration = 30,000)

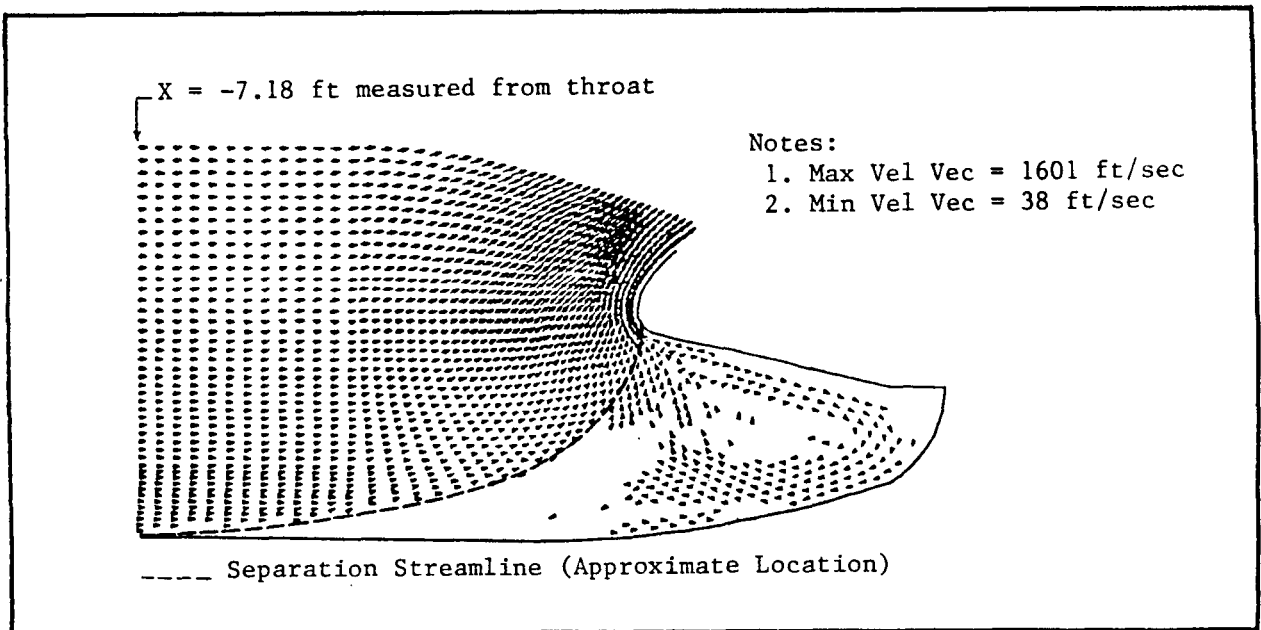
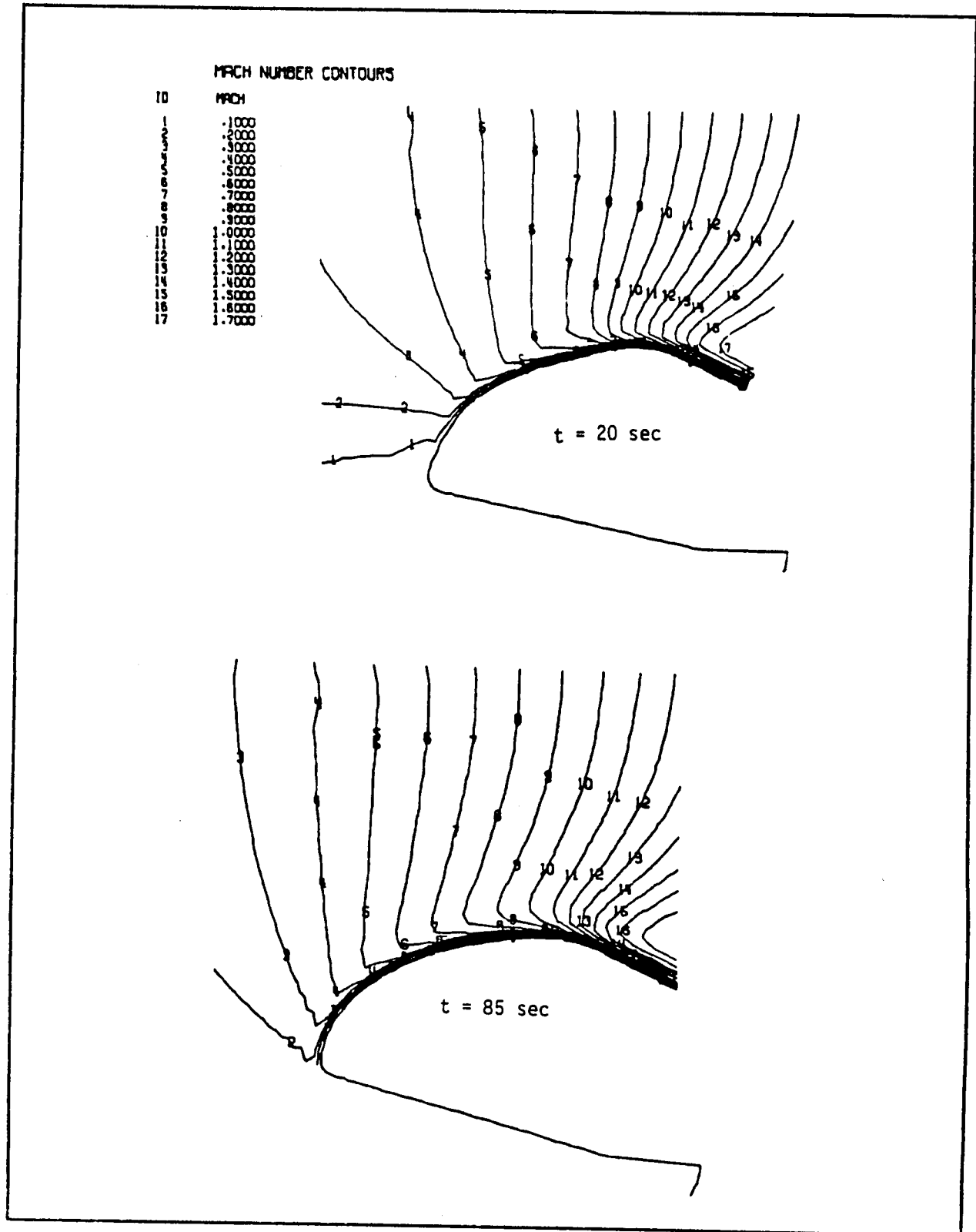


Fig. 16 GIM Code Calculated Velocity Vector Field
at t = 85 sec (Iteration = 30,000)

From the GIM code computational nodal descriptions, the upstream locations of the boundary layer separations are found to be approximately seven feet forward of the throat for both the $t = 20$ and 85-sec cases. The computed flow fields, separation streamlines, and separation points agree qualitatively with the water table test results of Ref. 4. The computed upstream separation points are needed since any additional modeling of the throat region should include this separated flow region in order to ensure a valid numerical solution which conserves mass.

The nozzle region calculated Mach number and static pressure (P/P_o) contours at $t = 20$ and $t = 85$ sec are compared in Figs. 17 and 18, respectively. The Mach number and pressure contours presented in Figs. 17 and 18 show little difference in the calculated nozzle internal flow field over the 403 and 404 rings and through the nozzle throat at $t = 20$ and $t = 85$ sec. The flow over the nozzle nose and through the nozzle throat is steady and well behaved. The only significant difference in the computed flow fields is the absence of vortex shedding in the $t = 20$ -sec solution. This was to be expected since the inhibitor protrusion is much less at $t = 20$ sec.

The calculated HPM nozzle surface pressure distribution at $t = 20$ and $t = 85$ sec was derived from the calculated nozzle pressure fields presented earlier. Only the surface pressure is of consequence since adiabatic wall boundary conditions are used; and since the flow is viscous, the surface velocities are zero. Since the surface pressure is important for both erosion and pressure loading of the nozzle components, both pressure profiles and integrated pressure loads over the surface of each nozzle component are presented. Figure 19 depicts the initial geometry of the nozzle carbon phenolic components. The $t = 20$ and $t = 85$ -sec nozzle surface geometry models are not shown, but will be only slightly different due solely to surface erosion. Figures 20 and 21 show the pressure profiles and integrated loads for the $t = 20$ and $t = 85$ -sec models, respectively. Note that the nose cap and most of the 402 ring are almost at stagnation pressure since they are adjacent to the quiescent flow region under the nozzle. Also, the integrated pressure loads are computed for the entirety of each axisymmetric ring.



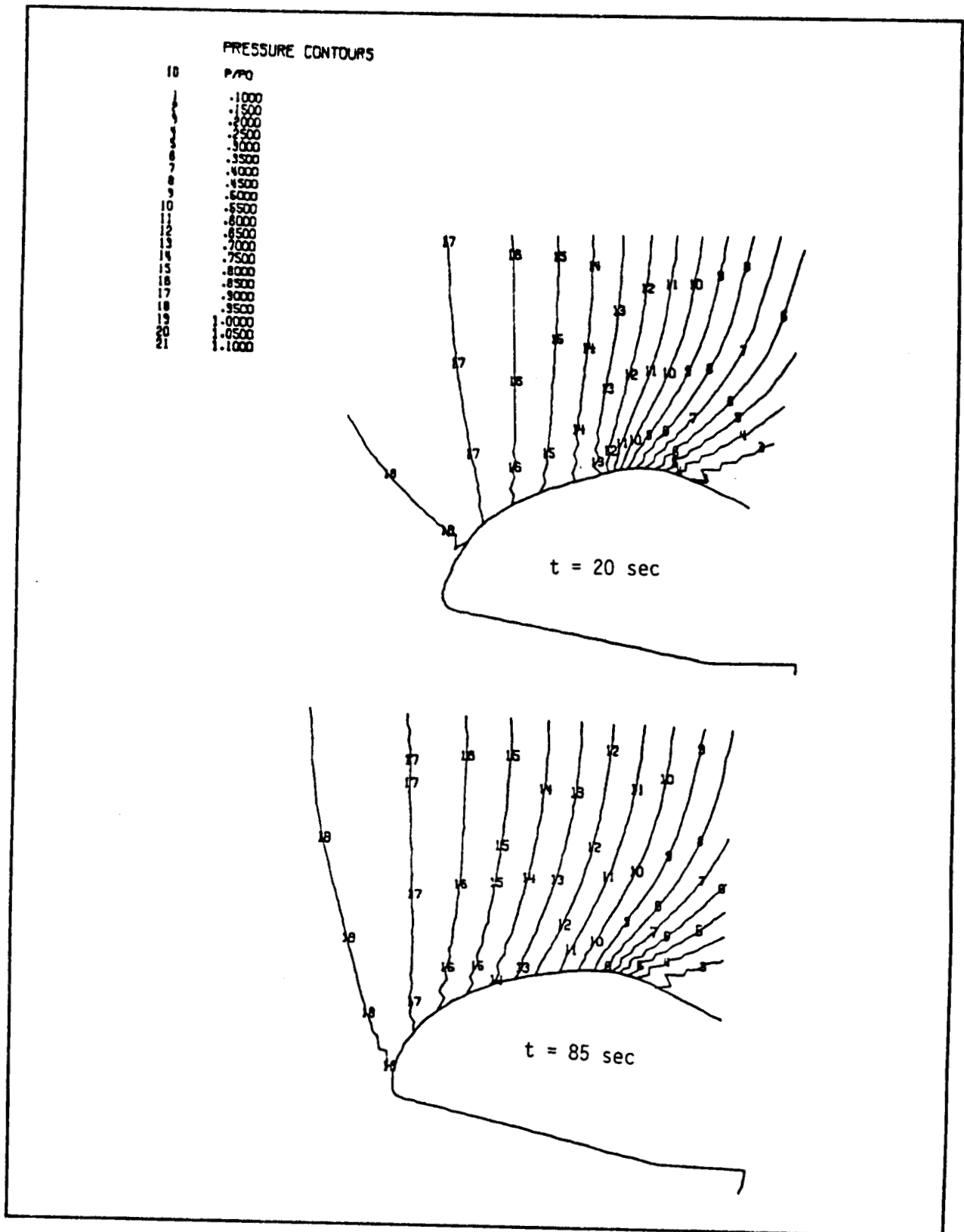


Fig. 18 GIM Code Calculated Static Pressure Contour Comparison
(Iteration 30,000) at t = 20 and t = 85 sec

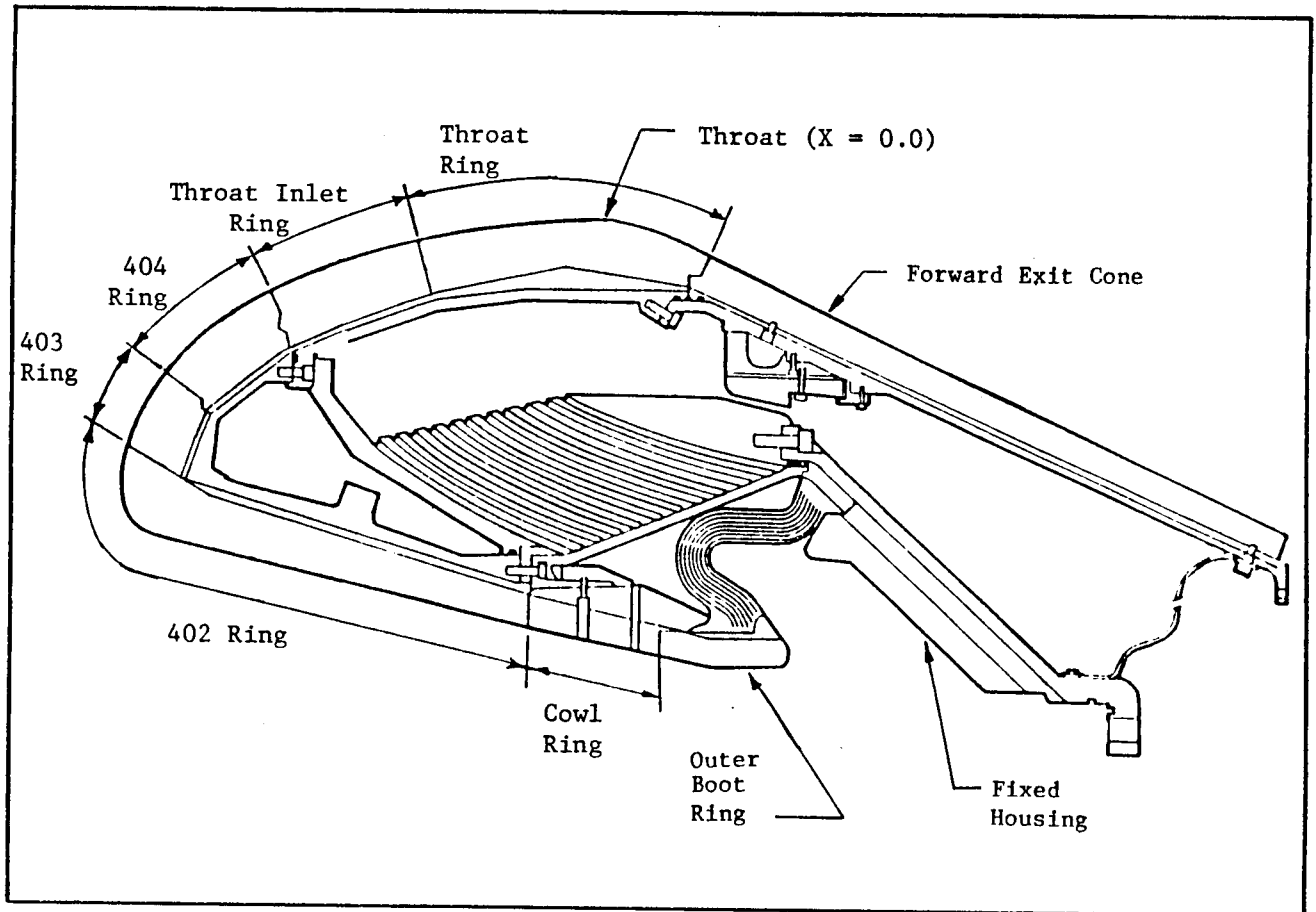


Fig. 19 HPM Nozzle Carbon Phenolic Components

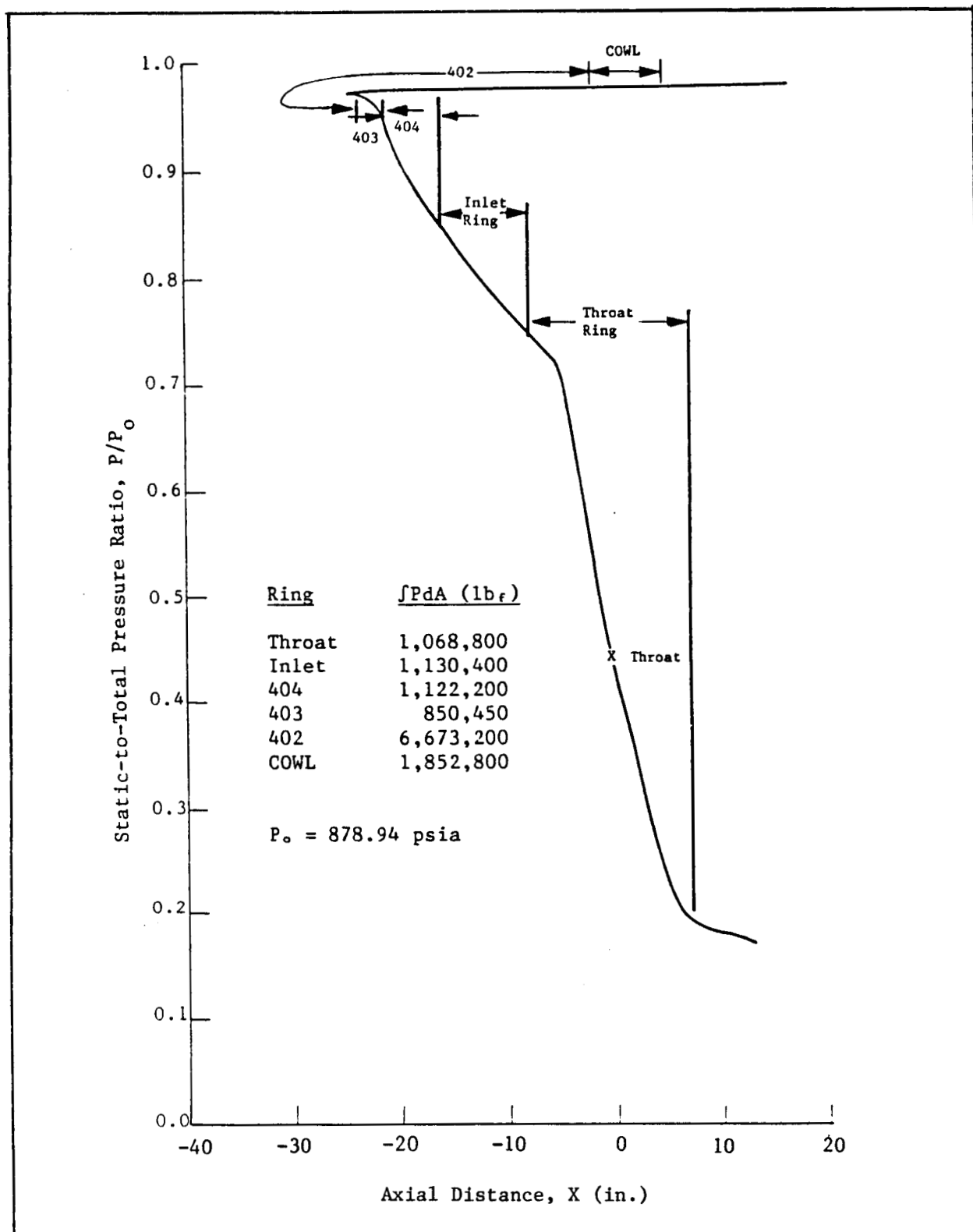


Fig. 20 GIM Code Calculated HPM Nozzle Surface Pressure Profile at $t = 20$ sec (Iteration 30,000)

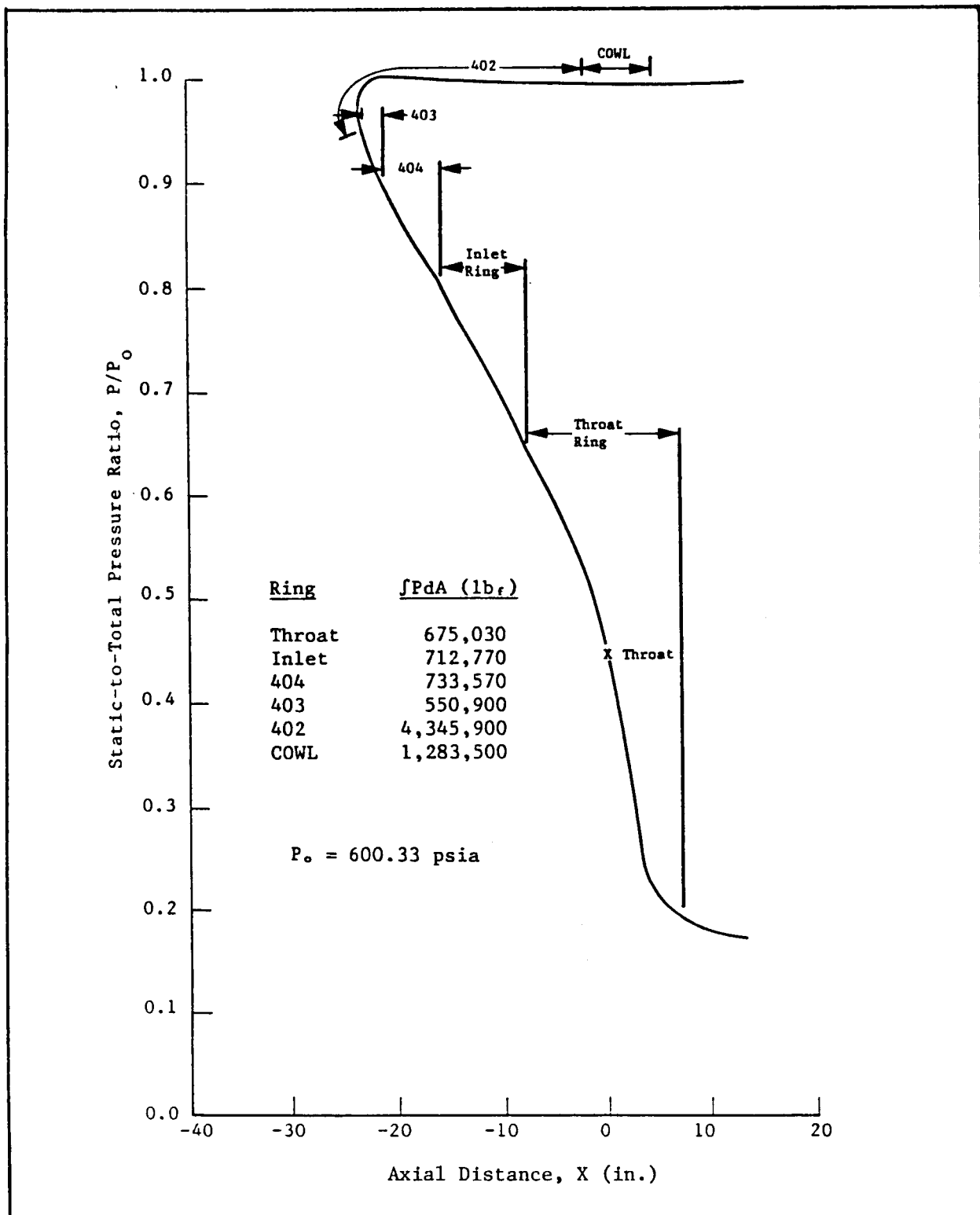


Fig. 21 GIM Code Calculated HPM Nozzle Surface Pressure Profile at $t = 85$ sec (Iteration 30,000)

2.2 THREE-DIMENSIONAL HPM 3.5-DEG GIMBALED NOZZLE FLOW FIELD AT $t = 9$ sec

2.2.1 Computational Grid and Initial Conditions

The general configuration of the computational region of the HPM aft segment extending to 10 ft upstream of the nozzle throat for the $t = 9$ sec gimbaled nozzle calculation is shown in Fig. 22. The nozzle wall contour for the +3.5-deg gimbal (0-deg plane) and -3.5-deg gimbal (180-deg plane) in addition to the gas properties are also shown in Fig. 22. The computational grid for this problem assumes a 180-deg plane of symmetry, contains 65,448 nodes, is divided into four zones, and contains 36 circumferential planes. The grid for this calculation is shown in Fig. 23 for the 0, 90, and 180-deg circumferential planes. In this calculation, mass addition from the propellant burning surface was considered. The velocity boundary condition at the propellant burning surface, the lower boundary shown in Fig. 22, is an injection velocity which varies based on axial location from approximately 10 to 12 ft/sec directed into the cavity normal to the boundary. The initial condition for the total pressure in the cylindrical port varies from 870.67 psia at the inlet plane to 866.66 psia at the nozzle throat. The initial conditions for the motor gas properties shown in Table 1 were provided by NASA-MSFC EP54 and were obtained using the computer program described in Ref. 2 modified by MSFC for treatment of the Space Shuttle HPM. In this solution a laminar fluid viscosity is assumed.

2.2.2 HPM Nozzle/Combustion Cavity Flowfield Computation and Results

● Core Flow and Nozzle Internal Flow

The PAID code calculation was carried out to 99,200 iterations. At this point in the calculation the flow in the cylindrical port and through the nozzle has reached a steady state solution. The flow under the nozzle nose and in the vicinity of the flexible boot/fixed housing exhibits unsteady behavior as was the case in the axisymmetric calculations presented in Section 2.1 of this report.

HPM AFT SEGMENT/NOZZLE REGION GAS PROPERTIES

t = 9 sec

Inlet Stagnation Pressure (psia)	870.67
Stagnation Temperature (R)	6361.0
Stagnation Density (lbm/ft ³)	0.38555
Ratio of Specific Heats	1.138
Molecular Weight (gm/gm-mole)	30.22861
Laminar Viscosity (lbm/ft-sec)	6.5×10^{-5}

Motor
Centerline

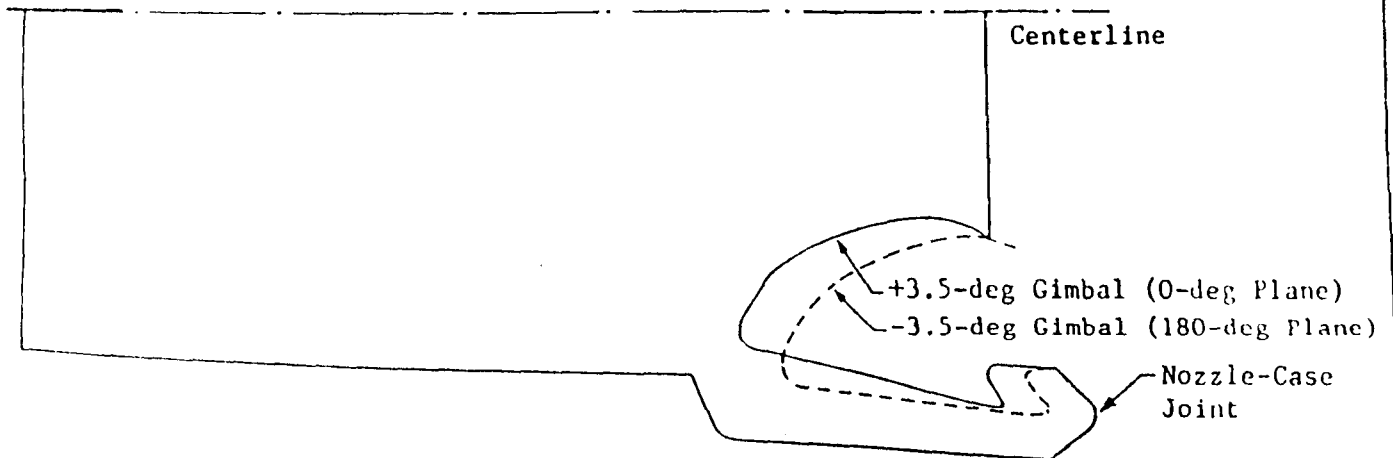


Fig. 22 HPM Gimbaled Nozzle Computational Region
and Gas Properties at t = 9 sec

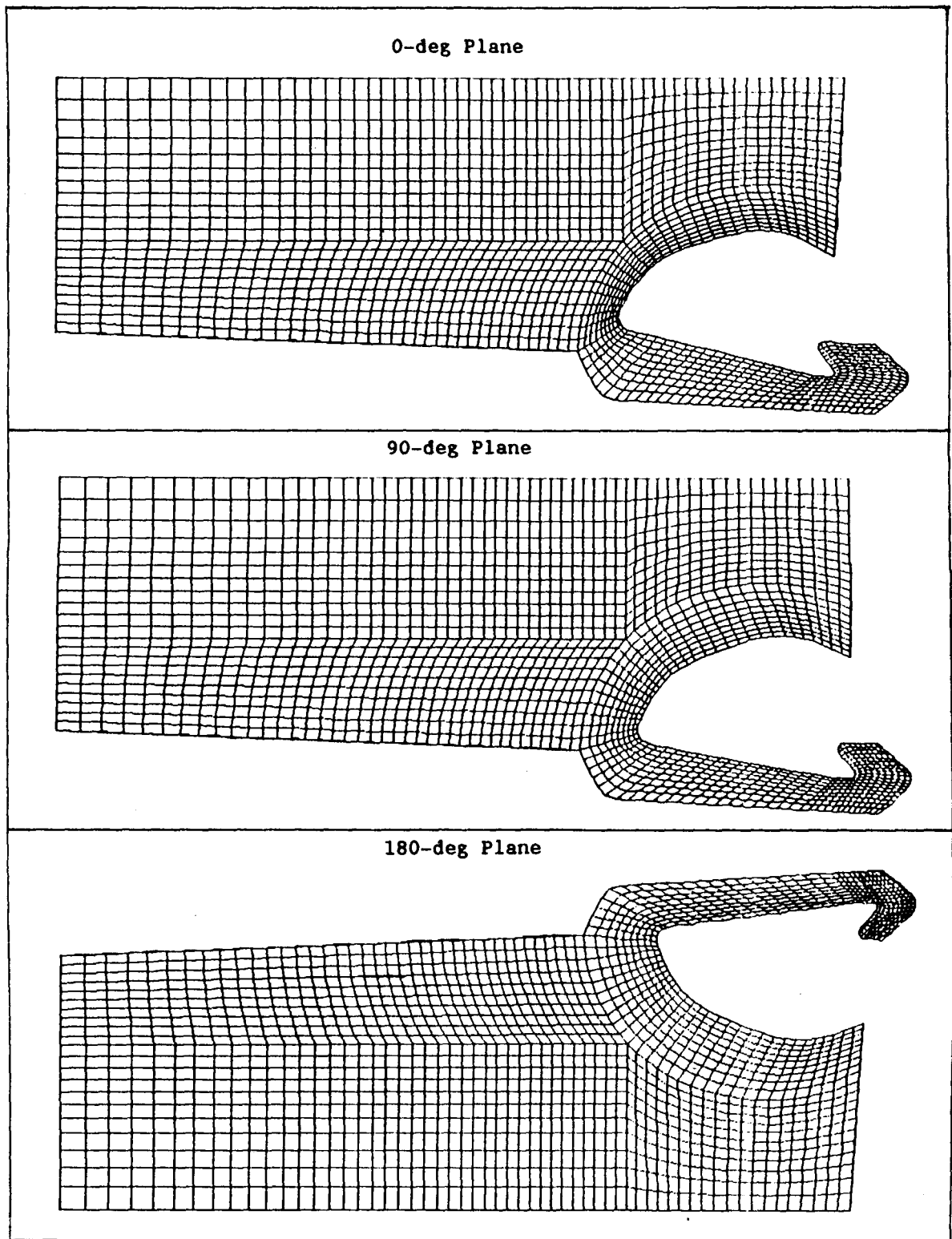


Fig. 23 HPM Gimbaled Nozzle Computational Mesh at $t = 9$ sec;
0, 90, and 180-deg Planes

Table 1 HPM 3.5-DEG GIMBALED NOZZLE FLOWFIELD ONE-DIMENSIONAL
INITIAL CONDITIONS AT $t = 9$ sec

Axial Station* (ft)	Stagnation Pressure (psia)	Axial Velocity (ft/sec)	Static Density (lbm/ft ³)	Mach Number	Propellant Flowrate (lbm/sec)
-10.0000	870.67	767.9	0.375773	0.2228	11,519.98
-8.1092	870.10	743.9	0.376101	0.2158	11,659.78
-7.5225	869.90	735.9	0.376218	0.2135	11,709.73
-5.9842	869.40	724.9	0.376261	0.2103	11,842.09
-4.5675	868.96	715.3	0.376287	0.2075	11,965.51
-4.4842	868.93	714.8	0.376275	0.2074	11,972.82
-2.8251	868.41	703.9	0.376426	0.2043	12,109.03
0.0	866.66	3337.4	0.236644	1.0	12,627.88
+1.10	866.66	4975.4	0.124951	1.558	12,627.88

*Referenced to nozzle throat plane.

The PAID code calculated velocity vector fields on the symmetry plane and at the 90 deg plane are shown in Figs. 24 and 25, respectively. The formation of the separation streamline surface and its asymmetric nature is indicated in Figs. 24 and 25 as the absence of velocity vectors near the propellant burning surface upstream of the nozzle nose.

The PAID code calculated combustion cavity and nozzle region Mach number and static pressure (P/P_0) contours for the symmetry and 90-deg planes are shown in Figs. 26 through 29. The static pressure contours shown in Figs. 28 and 29 are non-dimensionalized by the inlet plane stagnation pressure ($P_0 = 870.67$ psia) shown in Fig. 22. Notice that the flow in the region under the nozzle nose and in the vicinity of the flexible boot/fixed housing is unsteady and at near stagnation pressure. The PAID code nozzle surface grid and calculated nozzle surface static pressure (P/P_0) contours from the nozzle nose through the throat to the aft end of the throat ring are shown in Fig. 30. The calculated nozzle surface static pressure contours which have been non-dimensionalized by the inlet plane stagnation pressure ($P_0 = 870.67$ psia) from the nozzle nose through the throat are steady and well behaved.

• Velocity Profiles

The axial velocity profiles developed by the solution in the core flow region at the inlet plane ($x = -10.0$ ft) and a typical downstream plane ($x = -3.85$ ft) are shown in Fig. 31. In this figure the PAID code calculated axial velocity profiles are compared to the Culick profile found in Ref. 5. The calculated axial velocity profile at the inlet plane is typical of flow near the entrance of a pipe and as the flow progresses downstream a laminar profile develops which is the result of the laminar viscosity model used in the analysis.

2.2.3 HPM Nozzle/Case Joint Region Flowfield Computation and Results

The calculation of the nozzle/case joint region flow field is a difficult problem. The flow in this embedded region characterized by low velocities, high viscosity, and is nearly incompressible. Also this region will be the last portion of the entire flowfield to reach steady state or near steady state.

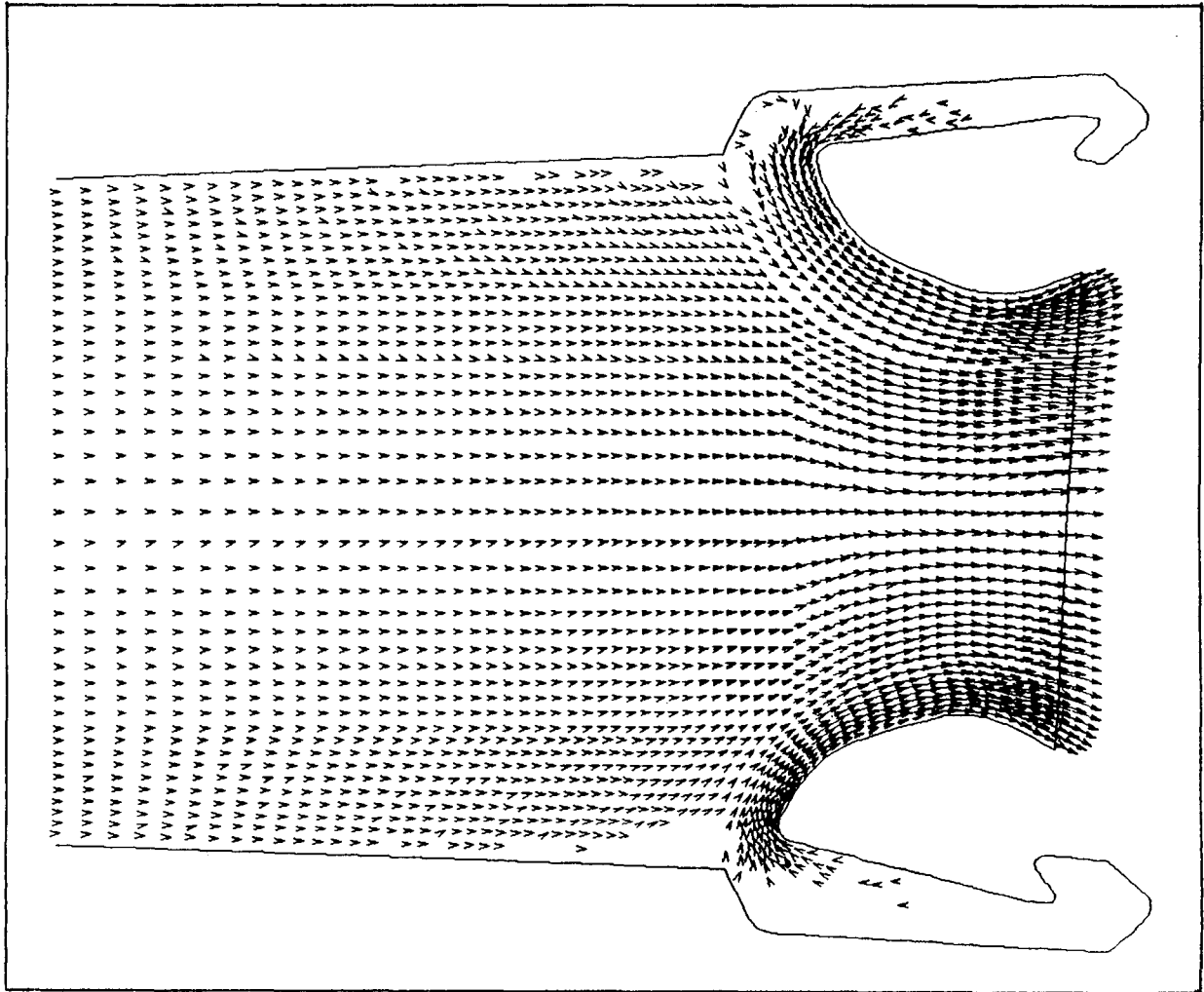


Fig. 24 PAID Code Calculated Velocity Vector Field, Symmetry Plane,
HPM 3.5-deg Gimbaled Nozzle at $t = 9$ sec, Iteration 99,200

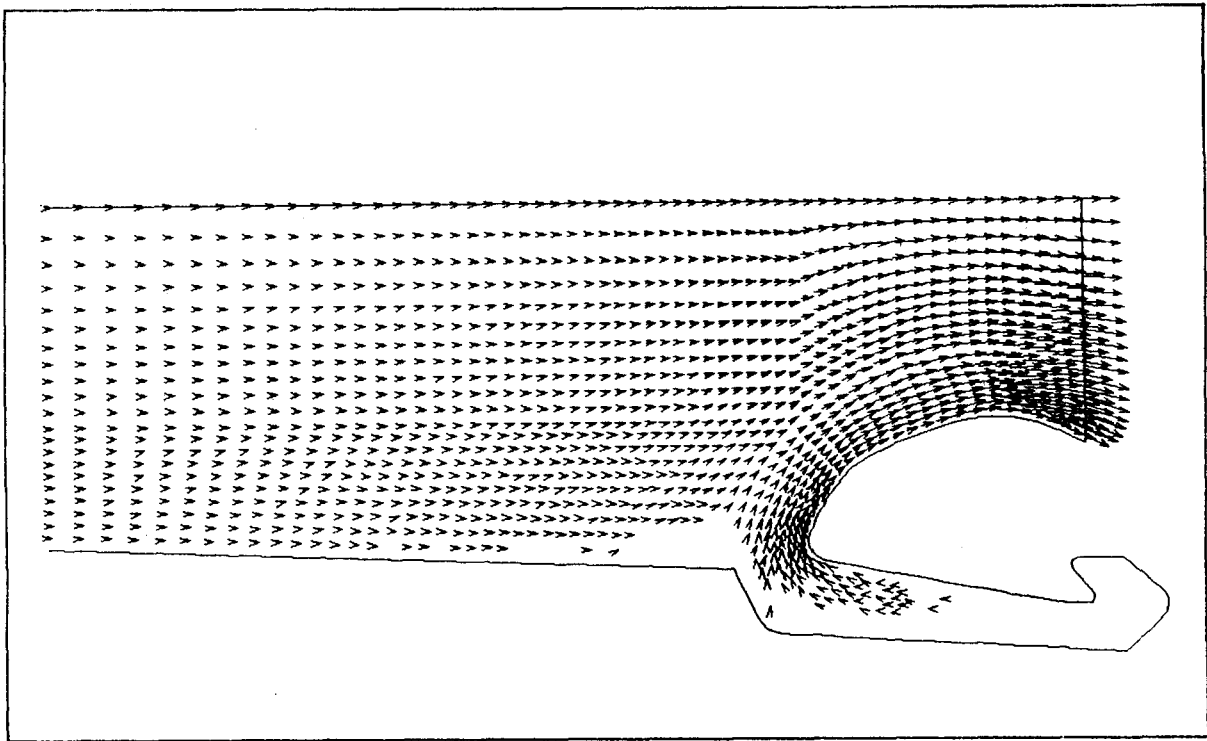


Fig. 25 PAID Code Calculated Velocity Vector Field, 90-deg Plane,
HPM 3.5-deg Gimbaled Nozzle at $t = 9$ sec, Iteration 99,200

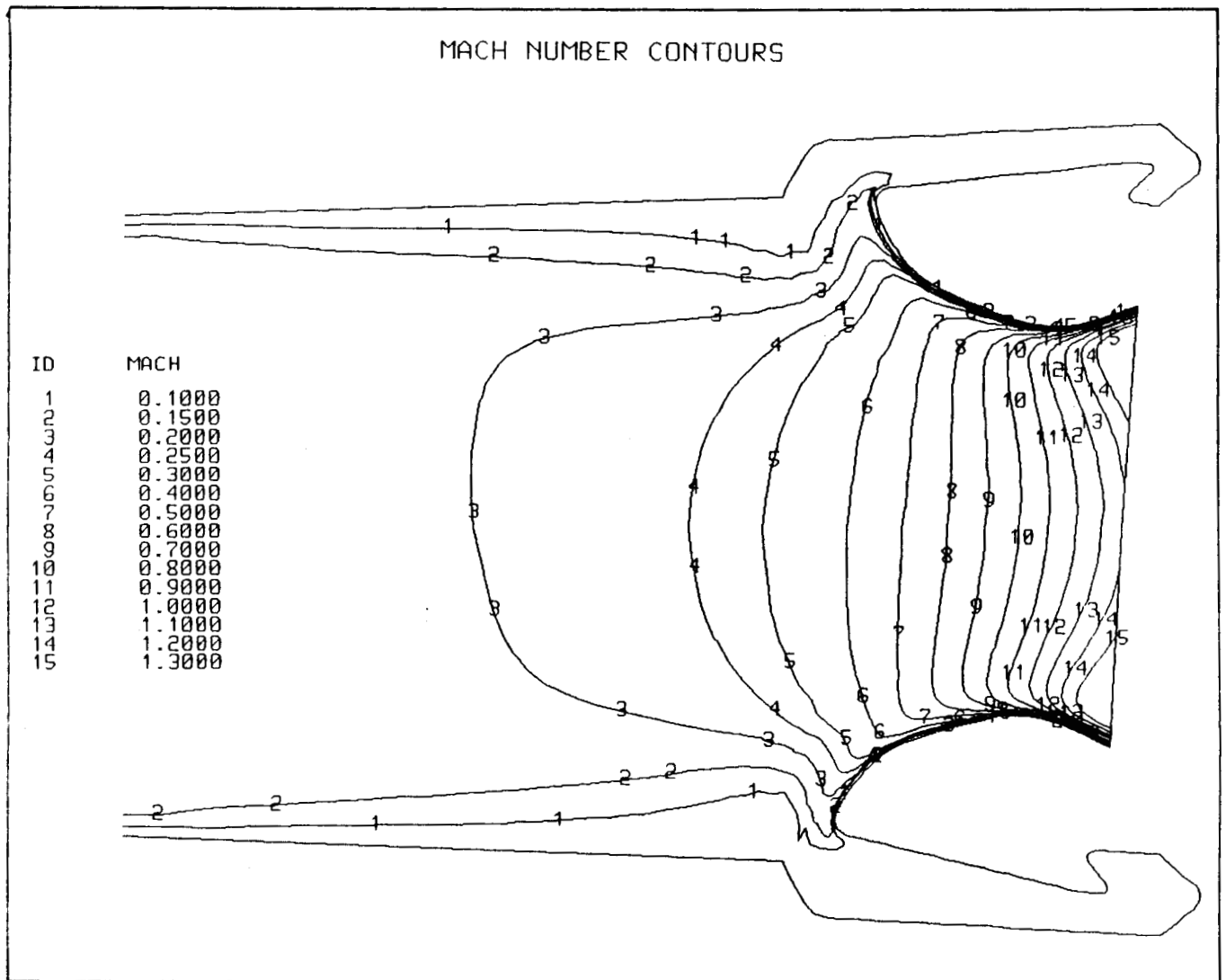


Fig. 26 PAID Code Calculated Mach Number Contours, Symmetry Plane, HPM 3.5-deg Gimbaled Nozzle at $t = 9$ sec, Iteration 99,200

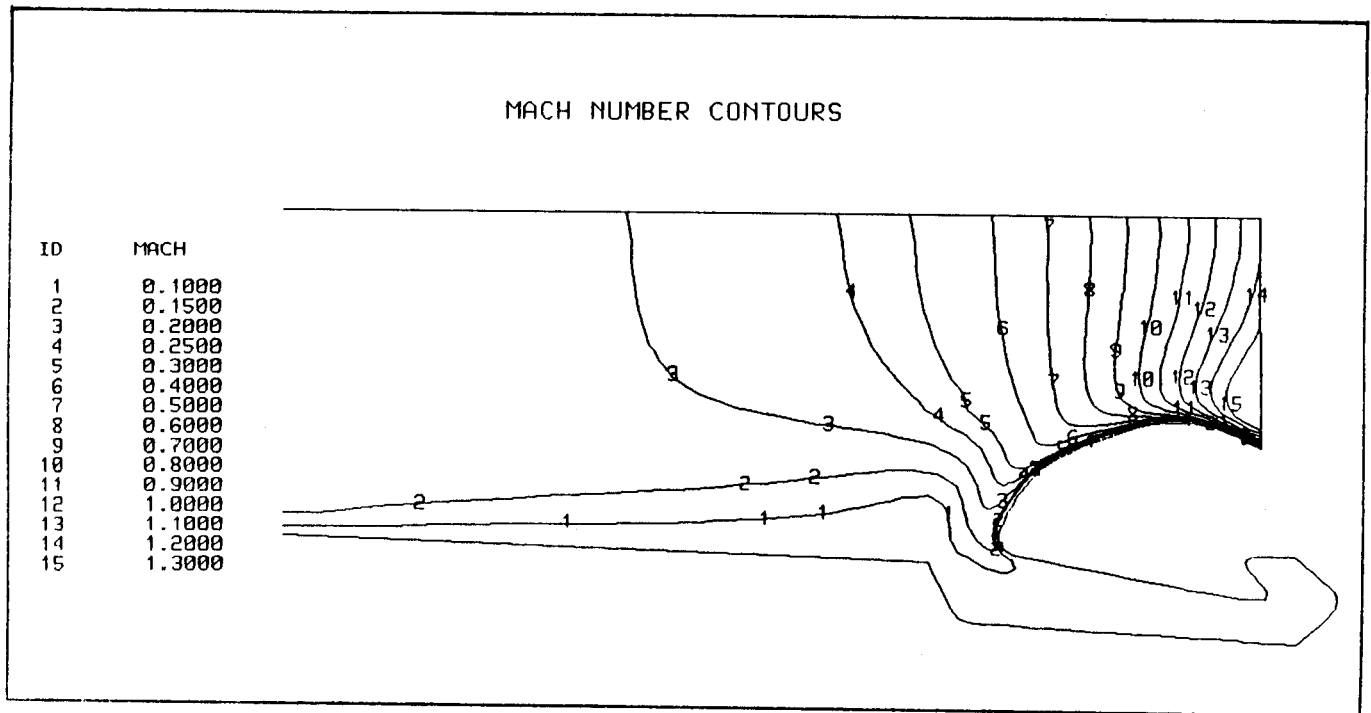


Fig. 27 PAID Code Calculated Mach Number Contours, 90-deg Plane,
HPM 3.5-deg Gimbaled Nozzle at $t = 9$ sec, Iteration 99,200

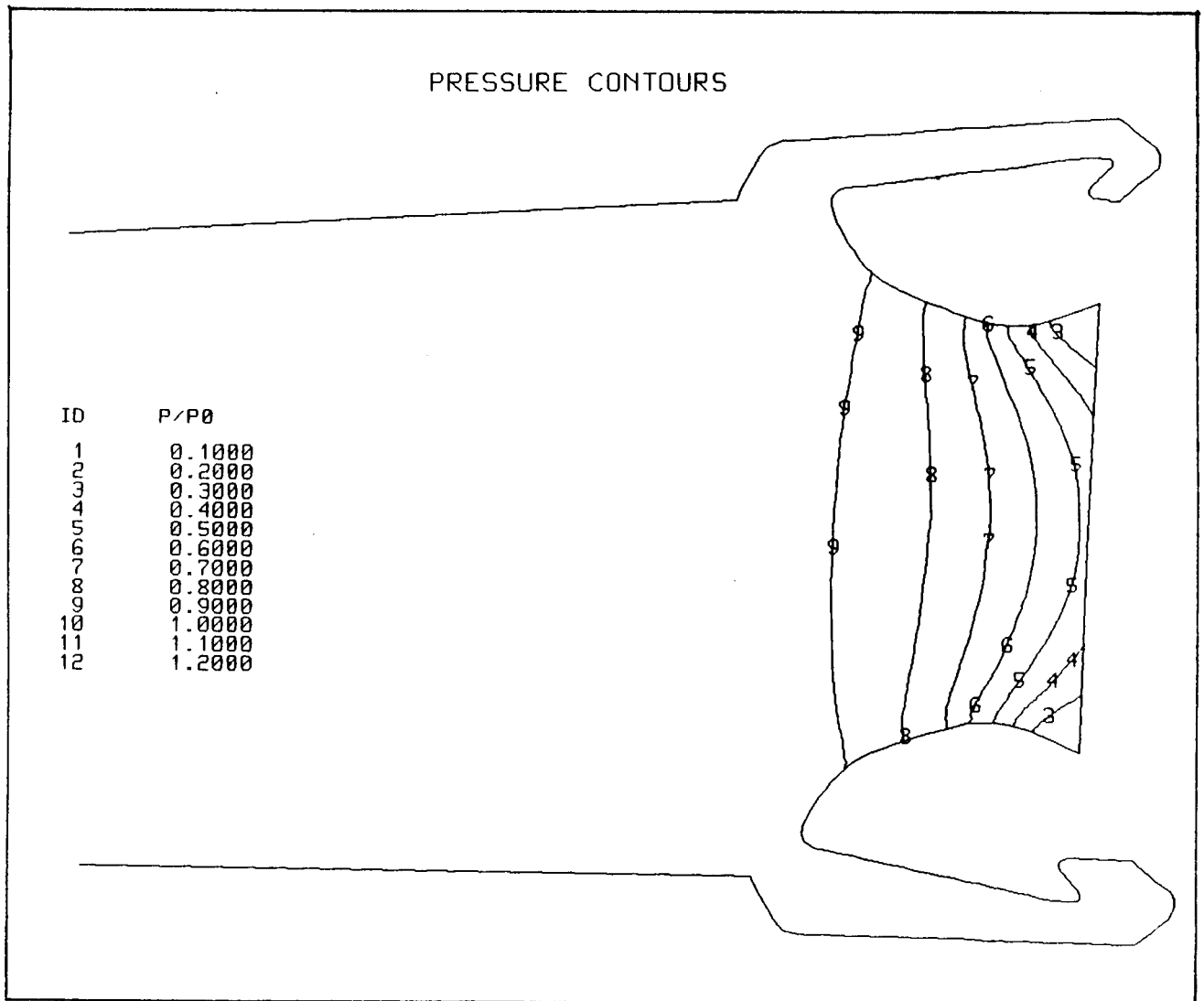


Fig. 28 PAID Code Calculated Static Pressure Contours, Symmetry Plane, HPM 3.5-deg Gimbaled Nozzle at $t = 9$ sec, Iteration 99,200

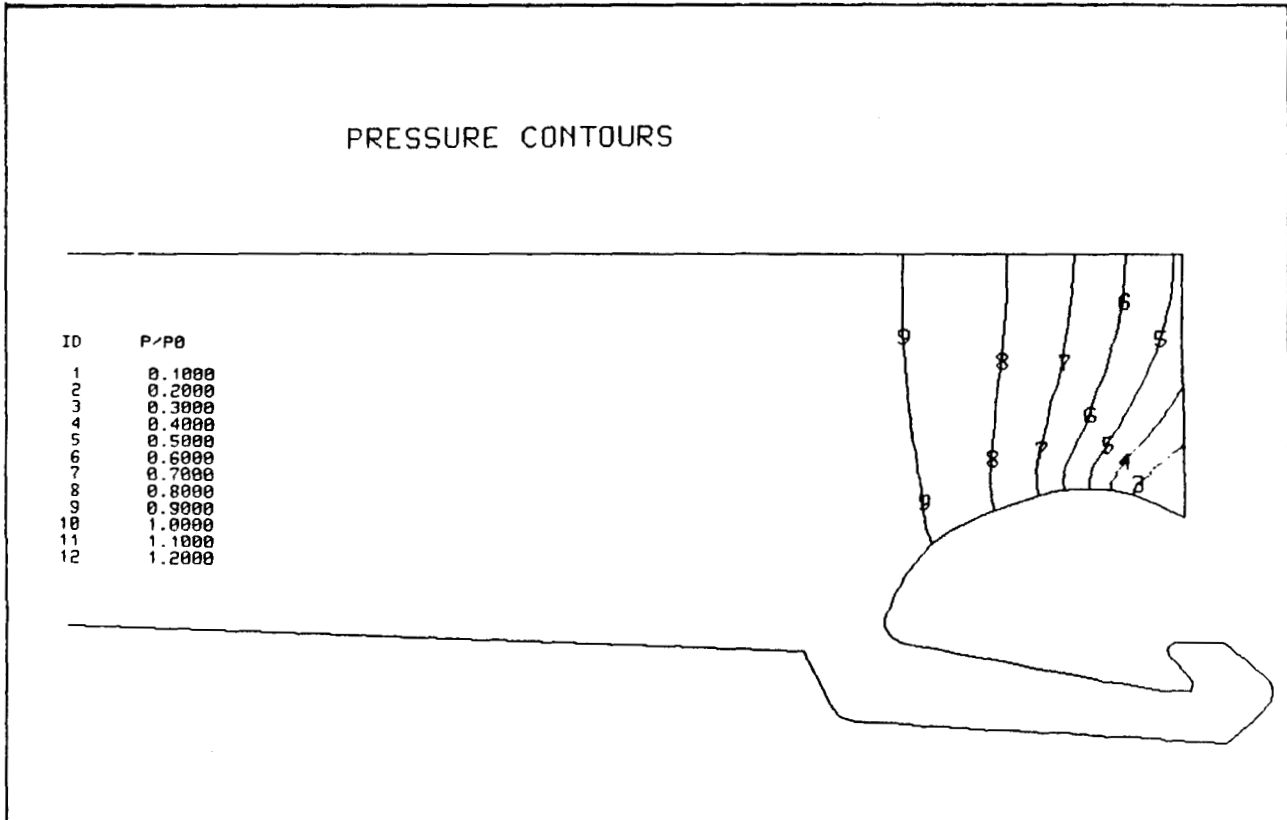


Fig. 29 PAID Code Calculated Static Pressure Contours, 90-deg Plane, HPM 3.5-deg Gimbaled Nozzle at $t = 9$ sec, Iteration 99,200

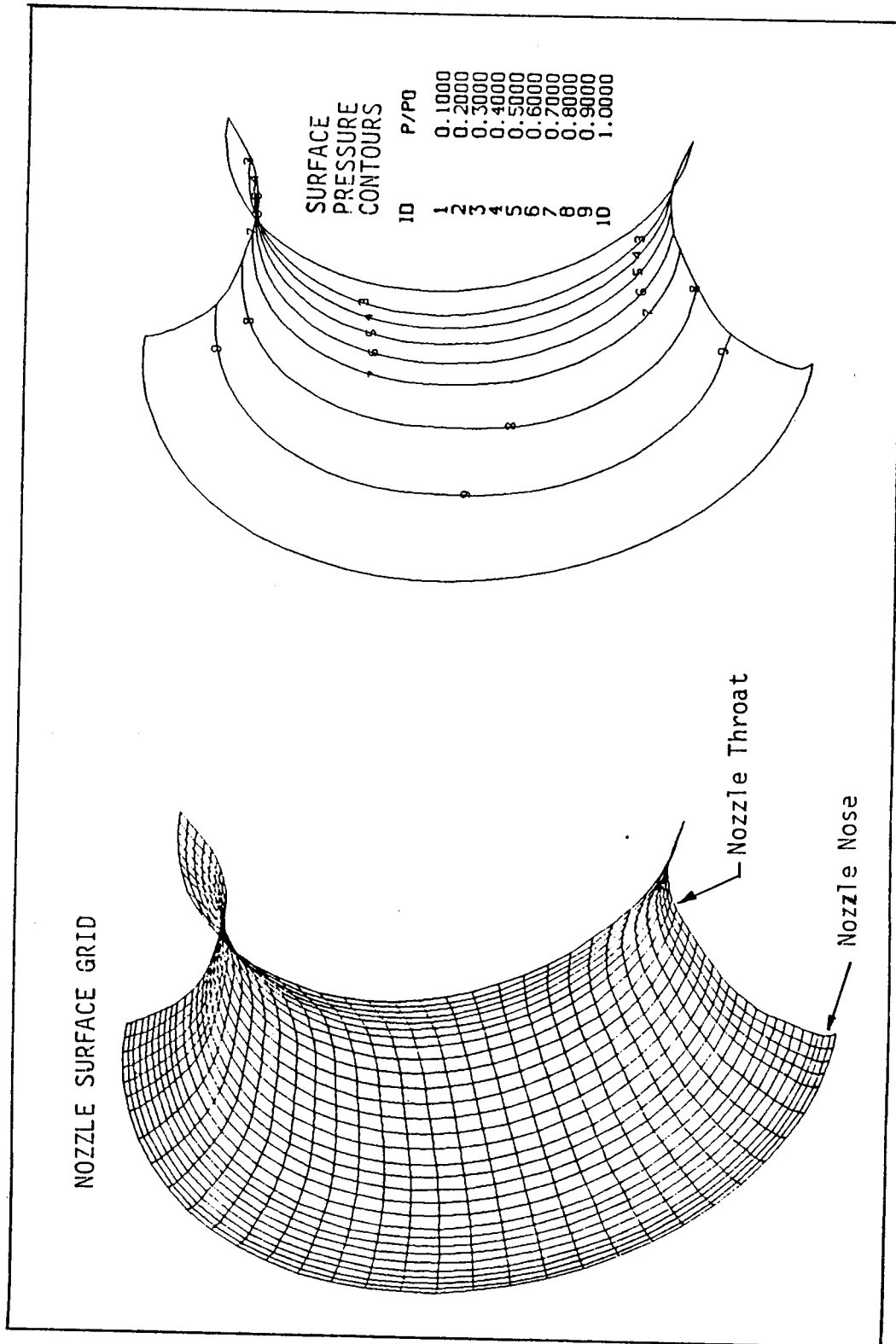


Fig. 30 PAID Code Calculated Nozzle Surface Static Pressure Contours, HPM 3.5-deg Gimbaled Nozzle at $t = 9$ sec, Iteration 99,200

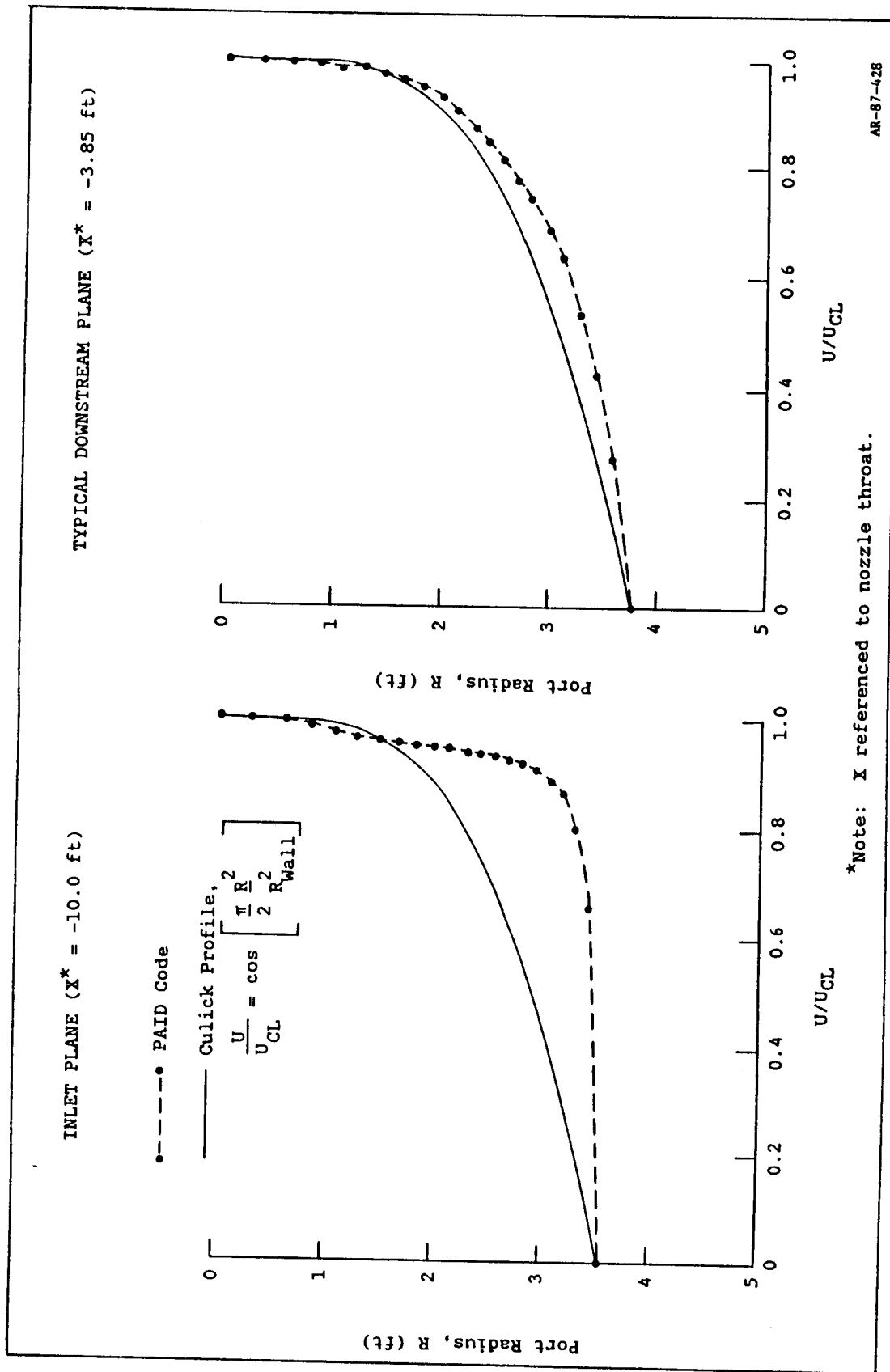


Fig. 31 Calculated Axial Velocity Profile Comparison,
PAID Code vs Culick Profile

The PAID code calculation for this region was carried out to 99,200 iterations. The location of nozzle/case joint and the general configuration of this region is shown in Fig. 22. The configuration of the flexible boot in the extended (0-deg plane) and contracted (180-deg plane) positions was estimated based on engineering judgment since little information is available concerning the geometry of the flexible boot as a function of nozzle gimbal angle. A large number of computational mesh points (6834 nodes) were concentrated in the area of the flexible boot, fixed housing, nozzle/case joint, and case insulation to capture the flow in this region.

• Nozzle/Case Joint Flowfield Solution

The flow under the nozzle nose in the cavity leading to the nozzle/case joint region determines the upstream conditions for the flow in the nozzle/case joint region. The calculated velocity vector field maps under the nozzle nose and in the vicinity of the nozzle/case joint at the 0, 90, and 180-deg computational planes are shown in Fig. 32. Notice that in this figure the direction of flow at each computational plane is off the propellant burning surface and upstream towards the nozzle nose. The maximum velocities shown in Fig. 32 occur near the nozzle nose surface and vary linearly from 558. to 610. ft/sec at the 0 and 180-deg computational planes, respectively.

The computed Mach number contours under the nozzle nose and in the vicinity of the nozzle/case joint at the 0, 90, and 180-deg computational planes are shown in Fig. 33. In this figure the maximum Mach number of 0.16 occurs at the 0, 90, and 180-deg computational planes near the nozzle nose just off the nozzle surface.

The computed static pressure contours (P/P_0) under the nozzle nose and in the vicinity of the nozzle/case joint at the 0, 90, and 180-deg computational planes are shown in Fig. 34. These results indicate that the static pressure in this region varies between 96 and 98% of stagnation ($P_0 = 870.67$ psia). The static pressure in this region is nearly constant and varies only two percent throughout the region.

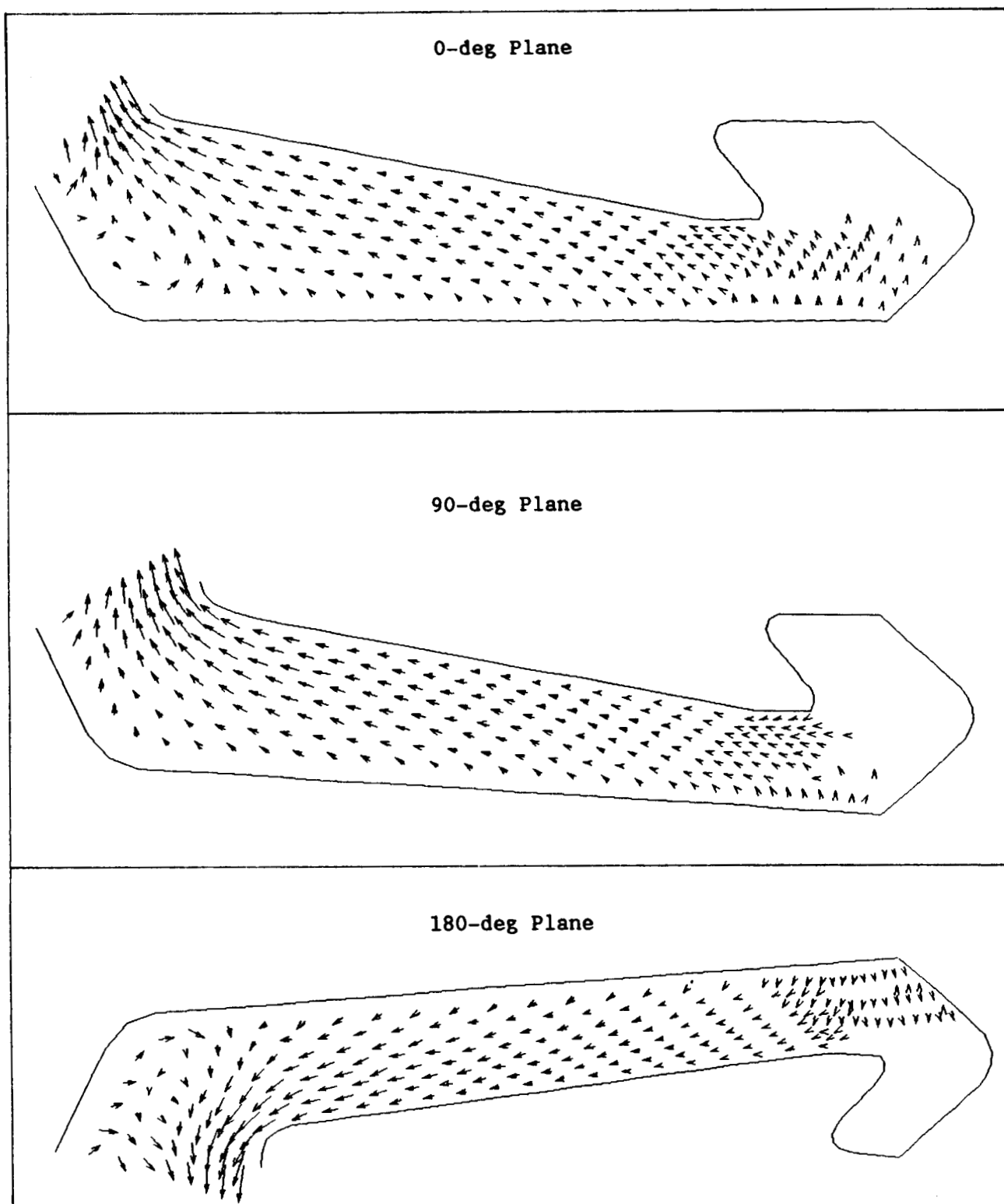


Fig. 32 PAID Code Calculated Velocity Vector Field; Nozzle/Case Joint Region; 0, 90, and 180-deg Planes; Iteration 99,200

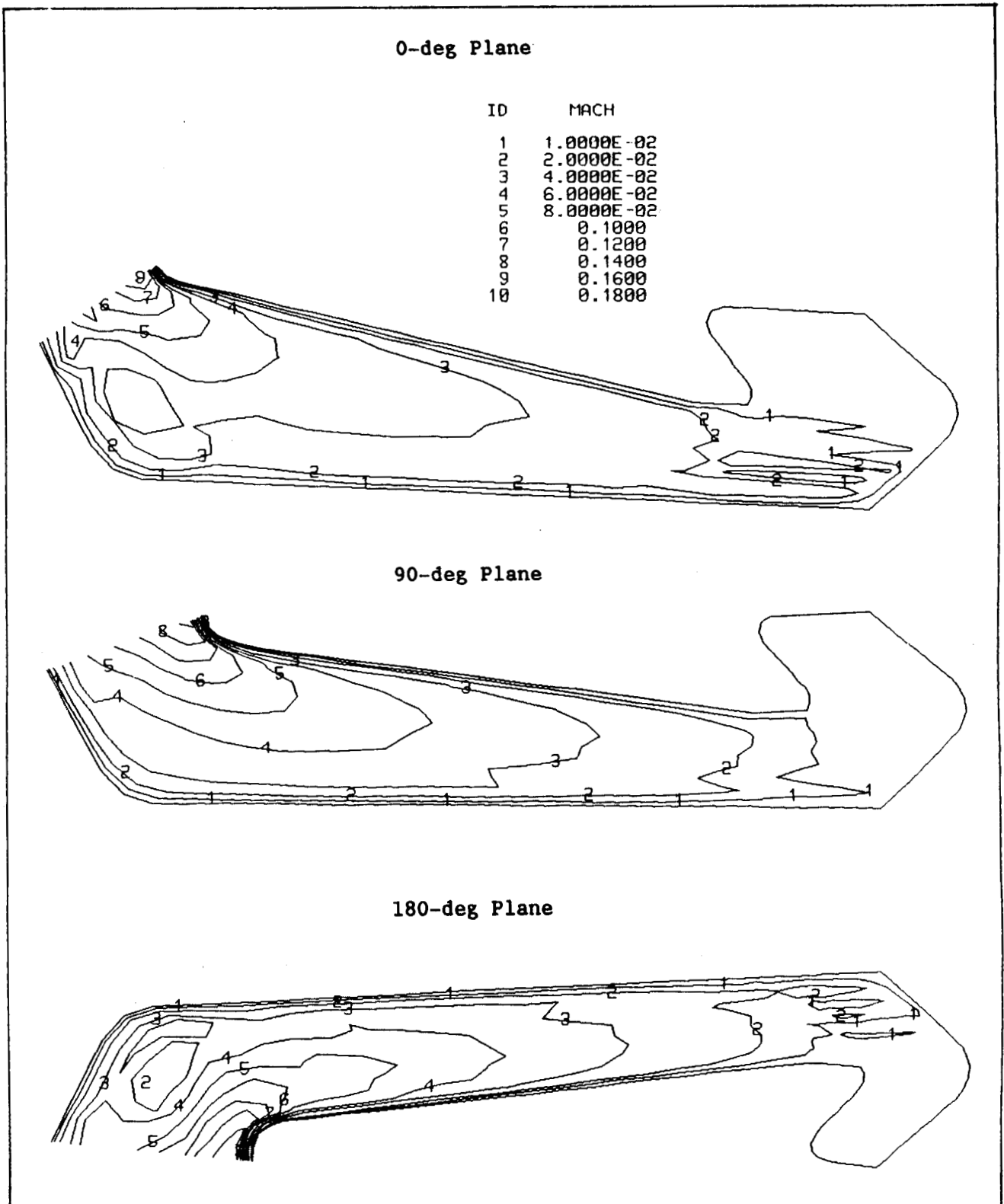


Fig. 33 PAID Code Calculated Mach Number Countours; Nozzle/Case Joint Region; 0, 90, and 180-deg Planes; Iteration 99,200

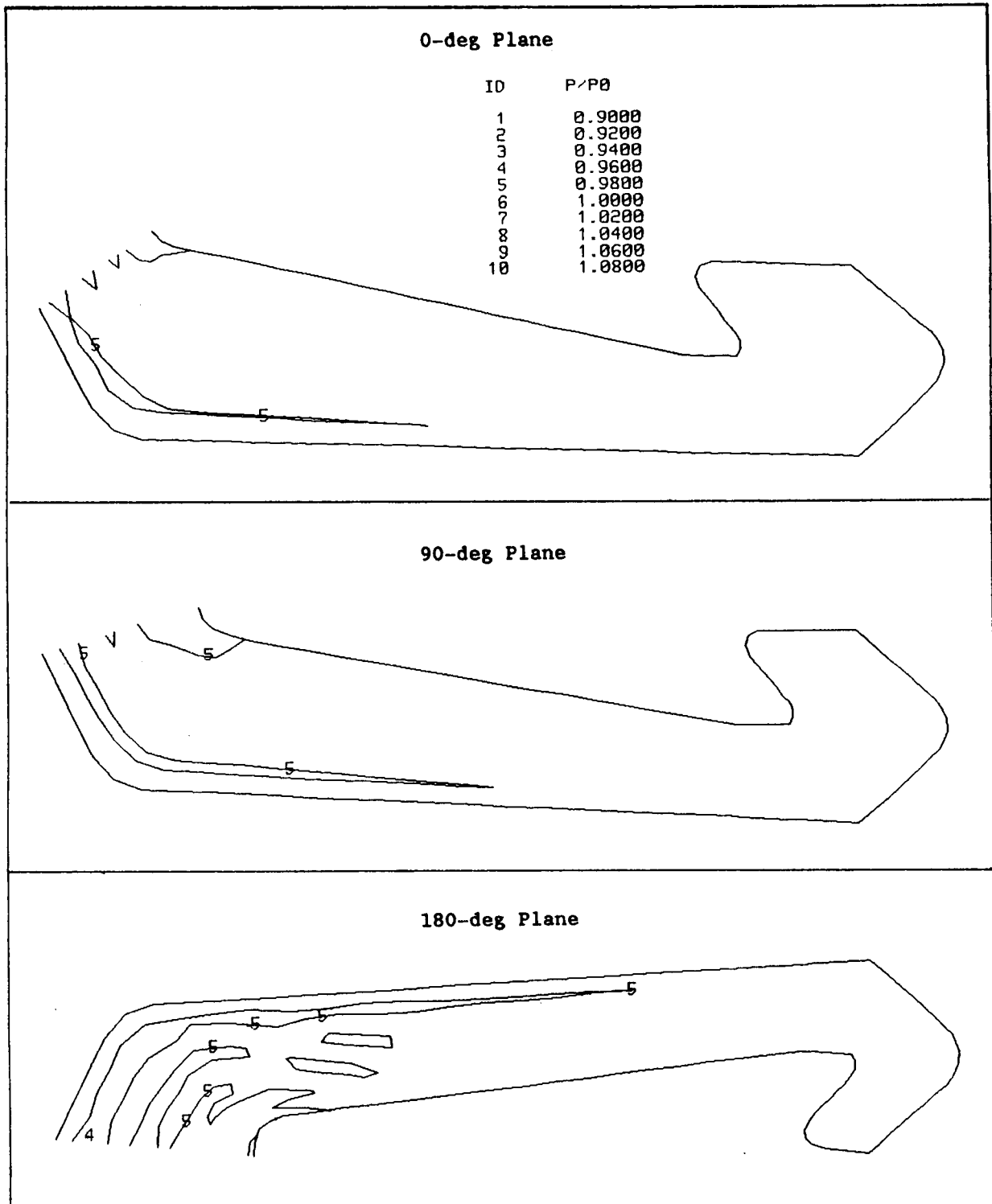


Fig. 34 PAID Code Calculated Static Pressure Contours; Nozzle/Case Joint Region; 0, 90, and 180-deg Planes; Iteration 99,200

The relaxation process for the flow field in the nozzle/case joint region can be illustrated by observing the calculated surface static pressure distributions at the nozzle/case joint. The nozzle/case joint region surface grid is shown in Fig. 35. This is a view of the surface grid looking aft into the cavity where the nozzle/case joint is located which shows the distribution of the 36 grid points in the circumferential direction. The nozzle/case joint calculated surface static distributions at iterations 38,200 and 43,200 are shown in Fig. 36. In this figure the circumferential static pressure differential varies from 1.4 percent at iteration 38,200 to 1.2% at iteration 43,200. At this point in the relaxation process the solution has not reached steady state in the nozzle/case joint region and is characterized by pressure waves which are moving back and forth in the circumferential direction between the 0 and 180-deg computational planes.

After 99,200 iterations the calculated nozzle/case joint surface static pressures are varying periodically in time about a mean value of 124,290 lbf/ft^2 (863.13 psia) or 99.1% of the inlet plane stagnation pressure. The amplitude of the periodic variation about the mean value of 124,290 lbf/ft^2 is very small ($\pm 2 \text{ lbf/ft}^2$). By taking the arithmetic mean of the calculated pressures over the period of the variation (0.00042 sec) at each of the 36 circumferential grid point locations the circumferential nozzle/case joint surface static pressure distribution has been determined. These results indicate that the calculated circumferential differential static pressure referenced to the static pressure at the 0-deg location is -0.55 psia. The calculated nozzle/case joint circumferential surface static pressure differential distribution is shown in Fig. 37. In this figure the calculated results are compared to NASA-MSFC/SRS cold flow test results for a 3.5-deg gimbal nozzle angle at $t = 9$ sec. In the cold flow tests (Ref. 6) the effect of mass addition from the propellant burning surface was not considered as was the case in the calculation.

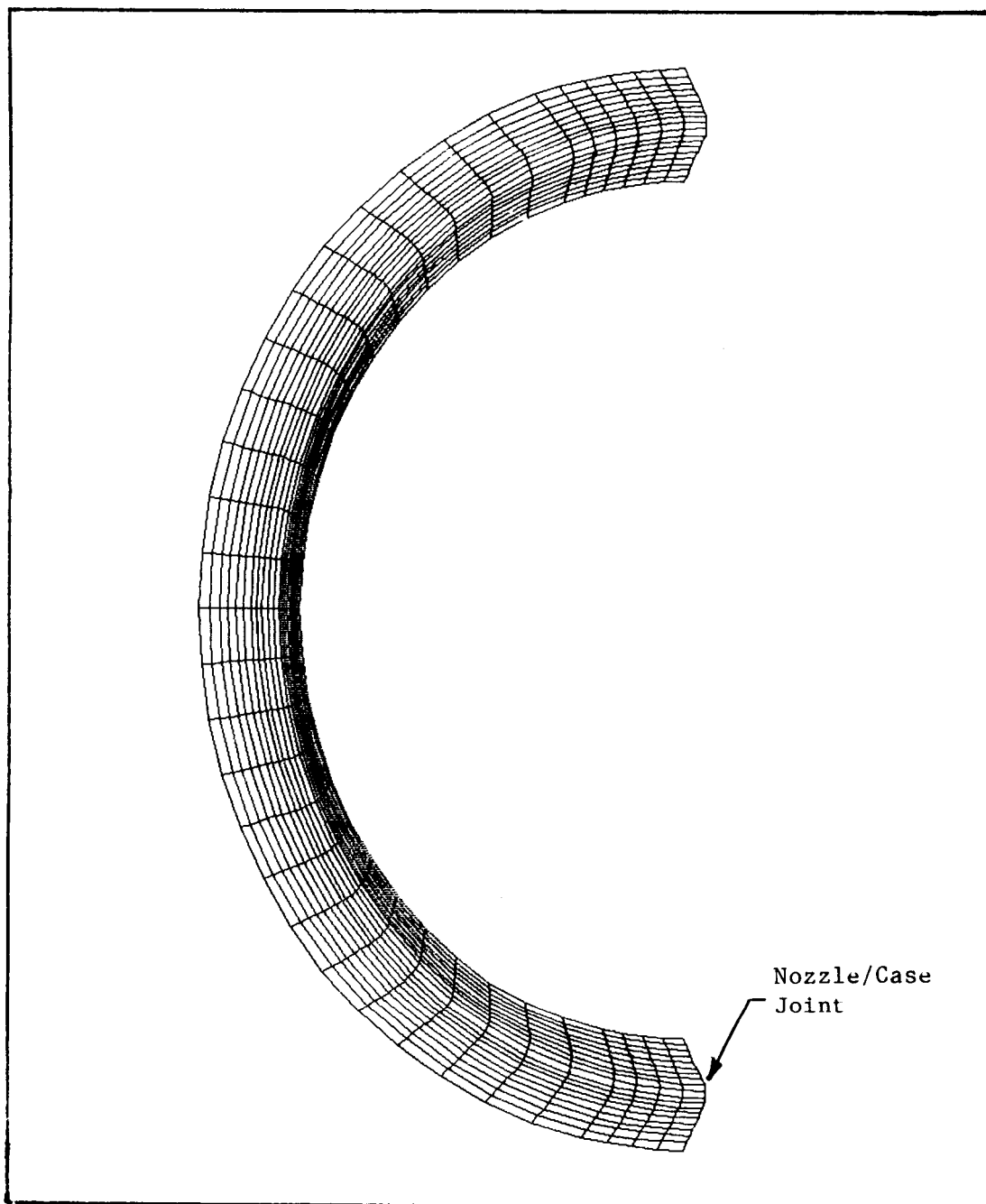


Fig. 35 Nozzle/Case Joint Region Surface Grid

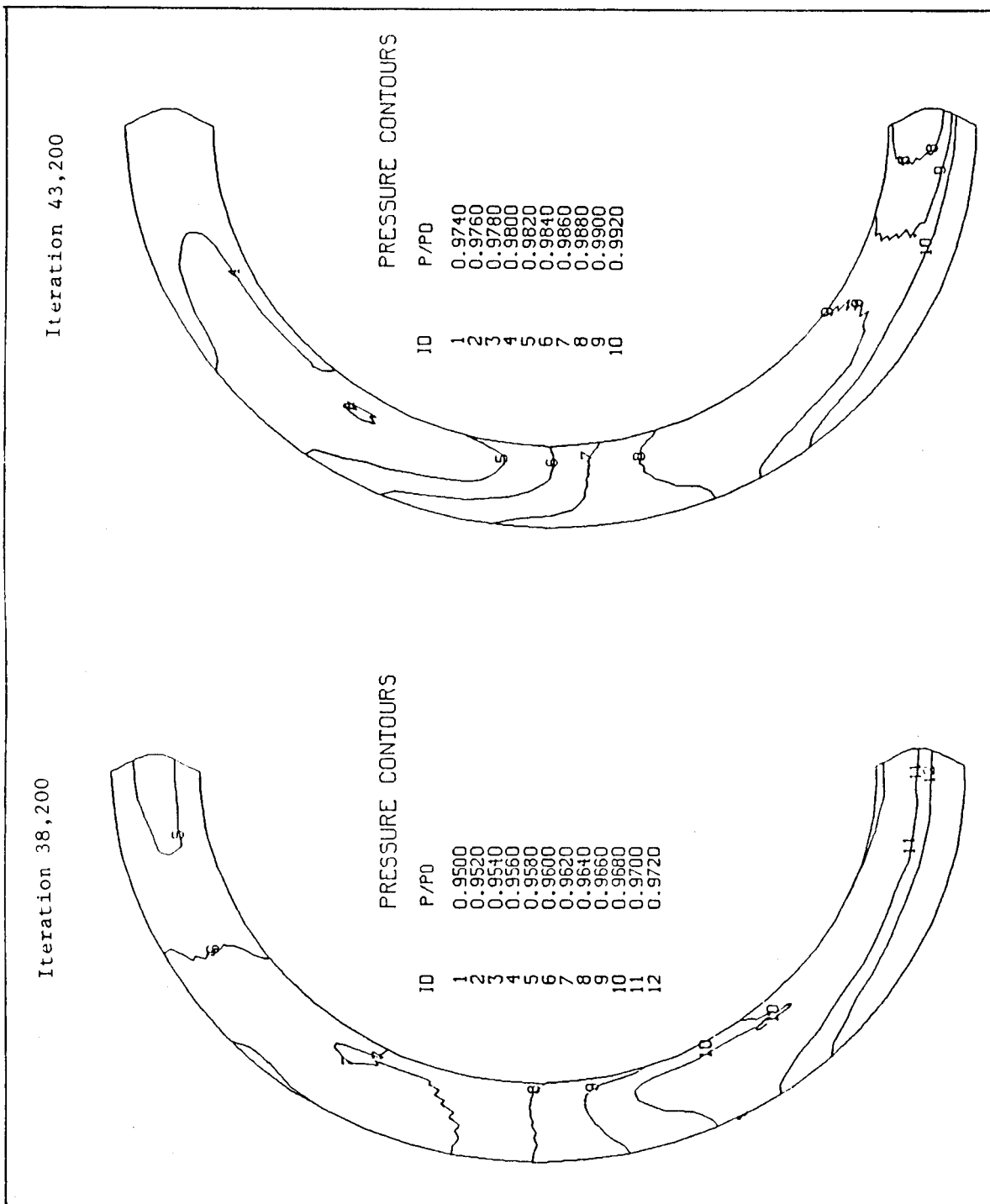


Fig. 36 Nozzle/Case Joint Region Calculated Surface Static Pressure Distributions, Iterations 38,200 and 43,200

In summary, the results of this calculation indicate that the flow field in the nozzle/case joint region exhibits unsteady behavior to the extent that the calculated nozzle/case joint surface static pressure varies periodically in time and the differential circumferential surface static pressure is approximately -0.55 psia. The calculated results are in reasonable agreement with cold flow measurements of the same configuration which were conducted without mass addition from the propellant burning surface.

Surface Circumferential Static Pressure Differential Distribution

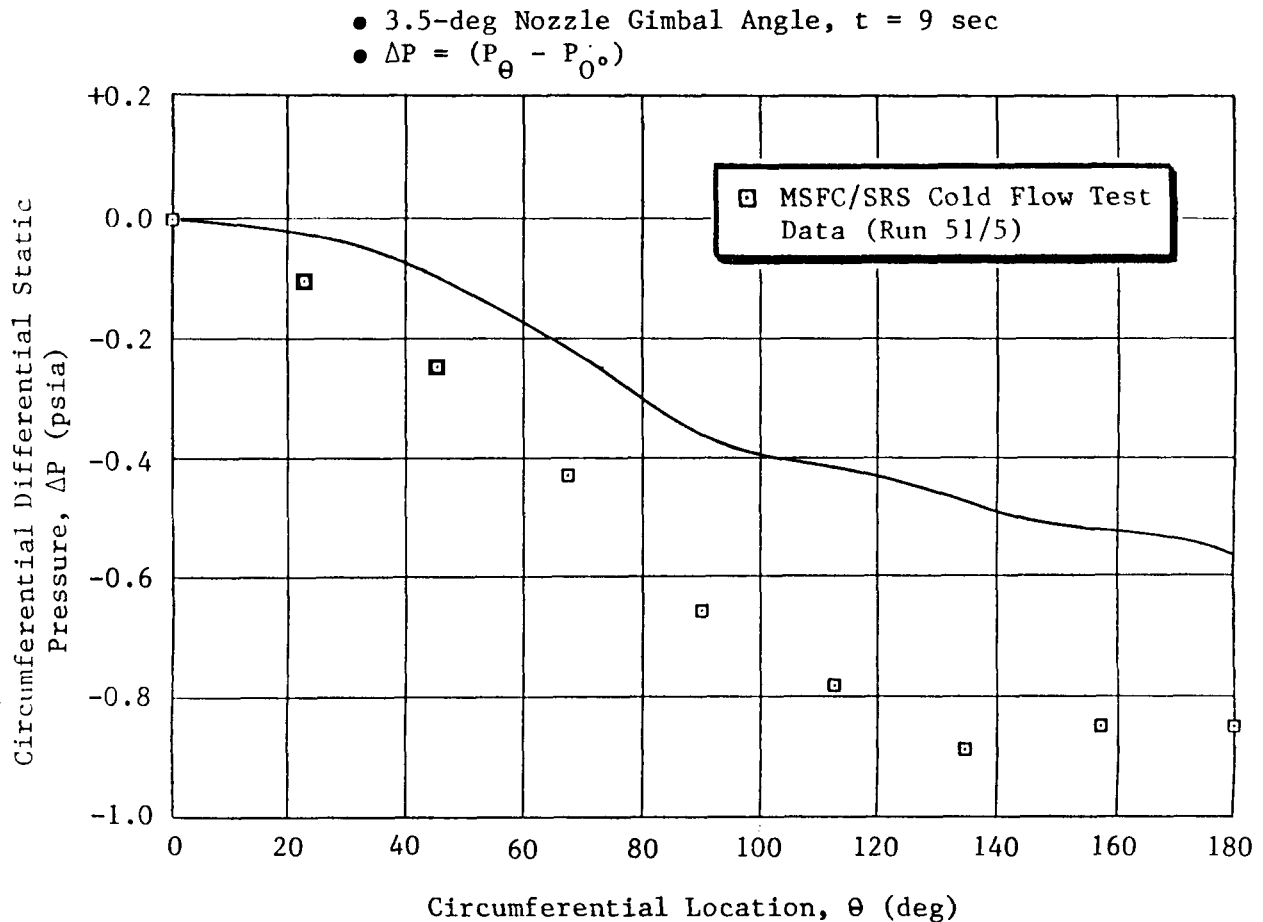


Fig. 37 Nozzle/Case Joint Calculated Circumferential Pressure Gradient

3. CONCLUSIONS

The two- and three-dimensional perfect gas flowfield solutions for the HPM aft segment and nozzle presented in this report have defined the flowfield characteristics at critical points in the motor burn time. The two-dimensional axisymmetric solution at $t = 85$ sec indicates that vortex shedding initiated by the aft segment forward inhibitor stub is a possible source of the acoustic activity noted at this burn time in motor flight and static test data. The two-dimensional axisymmetric solution at $t = 20$ sec does not predict the occurrence of vortex shedding which is consistent with the observed motor flight and static test history.

The three-dimensional 3.5-deg gimbaled nozzle solution at $t = 9$ sec indicates that the flow under the nozzle nose and in the region near the flexible boot and nozzle/case joint is unsteady and is characterized by low magnitude (less than 1.0 psia) circumferential pressure oscillations. Also for this gimbaled nozzle case the flow over the nozzle nose and through the throat is steady and essentially axisymmetric with respect to the gimbaled nozzle centerline.

Both the two- and three-dimensional solutions that have been developed indicate that the flow over the nozzle nose, 403/404 rings, and through the throat is steady and well behaved. There is no indication from the steady state flowfield results that the nozzle pocketing erosion which occurred on SRM-8A and -17B was initiated by a gasdynamic phenomenon. The specific findings of the two- and three-dimensional solutions are listed below.

3.1 FINDINGS OF THE 2D AXISYMMETRIC STEADY STATE GASDYNAMIC ANALYSIS

1. Calculations to date indicate that the flow field over the nozzle nose 403/404 rings, and throat is steady and well behaved.
2. At $t = 85$ sec, the calculation shows that vortex shedding occurs as a result of the forward inhibitor stub protrusion onto the aft segment flow field.
3. At $t = 20$ sec, the calculation does not predict the occurrence of vortex shedding off the forward inhibitor stub.
4. For both the $t = 20$ sec and $t = 85$ sec cases the calculated flow field under the nozzle nose and in the vicinity of the aft closure is a near stagnation region, unsteady, with low velocity recirculation patterns.

3.2 FINDINGS OF THE 3D 3.5-DEG GIMBALED NOZZLE STEADY STATE GASDYNAMIC ANALYSIS

1. The three-dimensional nozzle flow field calculation at $t = 9$ sec indicates that the flow over the nozzle nose, 403/404 rings, and through the throat is steady and well behaved.
2. The flow field in the nozzle/case joint region is unsteady and varies periodically with time.
3. The calculated nozzle/case joint surface static pressure varies periodically in time (± 0.02 psia) and the differential circumferential surface static pressure is approximately -0.55 psia.

REFERENCES

1. Pinoli, P.C., J.A. Freeman, and D.M. Berry, "High Performance Solid Rocket Motor (HPM) Nozzle Erosion - Final Report," LMSC-HEC TR D065599, 31 March 1987.
2. "Solid Propellant Rocket Motor Internal Ballistics Computer Program User's Guide," Report RK-TR-67-8, The Boeing Company, September 1967.
3. Test Report, "Space Shuttle Solid Rocket Motor Development Motor No. 5 Static Firing," Report TWR-13579, Morton Thiokol, Inc., Wasatch Division, Brigham City, Utah, May 1983.
4. Boraas, S., "Investigation of the STS-8A Nozzle Region Erosion," Report TWR-14413, Morton Thiokol, Inc., Wasatch Operations, Brigham City, Utah, June 1984.
5. Dunlap, R., R.S. Brown, P.G. Willoughby, R.C. Waugh, and A.M. Blackner, "Internal Flow Field Studies in a Simulated Port Rocket Chamber," CPIA Publication 412, Vol. 2, October 1984, pp. 119-137.
6. SRS Technologies Report, "Test Data Report Subscale Cold Flow Tests 3-D Aft Motor Case (SRM D MSFC 21, Phase 1)," SRS/STD-TR87-78, Huntsville, Ala., 31 July 1987.

DISTRIBUTION

Hercules Aerospace
Bacchus Works
P.O. Box 98
Magna, UT 84044-0098
Attn: D.D. Taylor, M/C N2WC1

Lockheed Missiles & Space Company, Inc.
3251 Hanover Street
Palo Alto, CA 94304-1187
Attn: F.W. Crossman, O/93-30, B/204
P.C. Pinoli, O/93-30, B/204
D.J. Wadiak, O/93-50, B/204

Lockheed Missiles & Space Company, Inc.
4800 Bradford Blvd.
Huntsville, AL 35807-1103
Attn: J.A. Freeman, O/59-91

Morton Thiokol, Inc.
Space Division
P.O. Box 524
Brigham City, UT 84302-0524
Attn: S. Boraas, M/S L21
D. Bright, M/S L22
D. Ketner, M/S L21
M. Salita, M/S 280
C. Saderholm, M/S E16

SRS Technologies
Systems Technologies Division
990 Explorer Blvd., N.W.
Cummings Research Park West
Huntsville, AL 35806
Attn: R.H. Whitesides

Air Force Astronautics Laboratory
Edwards AFB, CA 93523-5000
Attn: J. Levine (AFAL/DYCC)

Commander
DCASMA Birmingham
2121 8th Avenue North, Room 104
Birmingham, AL 35203-2376

National Aeronautics & Space Admin.
Marshall Space Flt Ctr, AL 35812
Attn: AS24D, five copies
AT01

T.F. Greenwood, ED33,
thirteen copies
P.R. Sulyma, ED33
S.H. Guest, ED33
D.L. Bacchus, ED33
J.E. Hengel, ED33
P.K. Tucker, ED32
D.F. Billings, ED32
G.T. Jamison, ED24
K.D. Coates, EE51
L.B. Powers, EE51
B.W. Shackelford, EP54
C.L. Martin, EP54
R.R. Fisher, EL56
R.L. Nichols, EH34
J.W. Thomas, Jr., SA42
J.D. Jordan, EM13B-11

NASA Scientific & Technical
Information Center
P.O. Box 8757
Baltimore/Washington International
Airport, MD 21240
Attn: Accessioning Department,
two copies